Eur. Phys. J. B **8**, 301–322 (1999)

THE EUROPEAN
PHYSICAL JOURNAL B
EDP Sciences

Detecting vorticity filaments using wavelet analysis: About the statistical contribution of vorticity filaments to intermittency in swirling turbulent flows

S. Roux[1], J.F. Muzy[2], and A. Arneodo[3,a]

[1] NASA's Goddard Space Flight Center, Climate and Radiation Branch (code 913), Greenbelt, MD 20771, USA
[2] Centre de Recherches Mathématiques, Université de Montréal, C.P. 6128, Succ. Centre-ville, H3C 3J7 Montréal (Quebec), Canada
[3] Centre de Recherche Paul Pascal, Avenue Schweitzer, 33600 Pessac, France

Received 27 July 1998 and Received in final form 23 November 1998

Abstract. Swirling turbulent flows display intermittent pressure drops associated with intense vorticity filaments. Using the wavelet transform modulus maxima representation of pressure fluctuations, we propose a method of characterizing these pressure drop events from their time-scale properties. This method allows us to discriminate fluctuations induced by just formed (young) as well as by burst (old) filaments from background pressure fluctuations. The statistical characteristics of these filaments (core size, waiting time) are analyzed in details and compared with previously reported experimental and numerical findings. Their intermittent occurrence is found to be governed by a pure Poisson's law, the hallmark of independent events. Then we apply the wavelet transform modulus maxima (WTMM) method to the background pressure fluctuations. This study reveals that, once removed all the filaments, the "multifractal" nature of pressure fluctuations still persists. This is a clear indication that the statistical contribution of the filaments is not important enough to account for the intermittency phenomenon in turbulents flows.

PACS. 02.50.-r Probability theory, stochastic processes, and statistics – 05.40.+j Fluctuation phenomena, random processes, and Brownian motion – 47.27.Gs Isotropic turbulence; homogeneous turbulence – 47.32.-y Rotational flow and vorticity

1 Introduction

Most experiments reported so far in three-dimensional fully developed turbulence attempted to characterize the statistical properties of either the velocity [1–8] or the dissipation [9–12] fields. The fluctuations of these two quantities are supposedly related by the so-called Kolmogorov's refined self-similarity hypothesis [13]. Experimental data were thus used to test the validity of this hypothesis as well as the relevance of various statistical cascade models [2–7, 12]. But these works only brought very limited information about the origin of turbulence. In particular, still a little is known about the existence, the dynamics and the specific role of coherent structures in three-dimensional turbulent flows [14–18]. Recently, the observation and the characterization of well organized structures have received some renewed interest from both a numerical [19–29] and an experimental [30–42] point of view.

Since the original numerical work of Siggia [19], several simulations have shown the existence of high vorticity regions structured in cylindrical shapes, vorticity filaments or vortex sheets [20–29]. When processing images of these regions of high vorticity concentration, one observes that low pressure regions correspond to vorticity filaments [22–26]. Moreover, when using conditional visualization technique involving vorticity ($\boldsymbol{\omega} = \boldsymbol{\nabla} \wedge \boldsymbol{v}$) and strain rate ($\sigma^2 = \frac{1}{2}\sum_{ij}(\frac{\partial v_i}{\partial x_j} + \frac{\partial v_j}{\partial x_i})^2$), one shows that the regions of both large vorticity and weak strain rate have the shape of elongated filaments [28]. In contrast, the regions with both large vorticity and large strain rate are flat layers with a shape of pancakes. Indeed the vorticity and the strain rate are connected by the relation [43]:

$$\int_V \omega^2 dV = \int_V \sigma^2 dV = \frac{1}{\rho\nu}\int_V \epsilon dV \ , \qquad (1)$$

where ν is the kinematic viscosity, ρ the density and ϵ the dissipation rate.

Equation (1) suggests that the intermittent spatial distribution of ϵ should be mirrored in some way in the intermittent spatial distribution of ω. But the dissipation field, likewise the vorticity field, requires the simultaneous recording of the three components of the velocity which is at the moment feasible for numerical simulations but hardly accessible experimentally. A very attractive alternative strategy consists in studying vorticity filaments

---

[a] e-mail: `arneodo@crpp.u-bordeaux.fr`

via direct measurement of pressure fluctuations [33–37]. Actually, in an incompressible fluid, it is well known that the pressure obeys a Poisson's equation derived by taking the divergence of the Navier-Stokes equations [30]:

$$\frac{2}{\rho}\Delta p = \omega^2 - \sigma^2 \; . \tag{2}$$

One can thus develop an analogy with electrostatics where the pressure corresponds to the potential resulting from negative and positive charges distributed in proportion to the square of vorticity and to the energy dissipation respectively. The regions of intense vorticity thus act as sources of low pressure and when vorticity predominates over dissipation they cause strong depressions.

Along the line of the above argument, Douady *et al.* [30] devised a direct visualization method of the low pressure regions which consists in seeding a medium (a water layer confined in a gap between coaxial contra-rotating disks) with small air bubbles which migrate through the pressure gradient towards the depression cores. Using this technique, they clearly evidenced the intermittent formation of bubble filaments in these turbulent Von Karman swirling flows which confirms that vorticity has a strong tendency to concentrate in tube-like structures. Experiments in similar closed rotating flow configurations were performed with fluids of various viscosities (diluted glycerol [33–37], water [30–37], helium [41,44–47]) in order to scan a wide range of Reynolds numbers. This bubble visualization technique has been further used in different experimental set-ups; let us mention that Villermaux *et al.* [40] have observed intense bulk vortical structures in a mean shear free, homogeneous, isotropic, stationary turbulence generated by oscillating grids. These rather qualitative visual observations were supplemented by pressure [33–37] and velocity [34,35,41,46,47] fluctuation measurements and also by the investigation of pressure-velocity correlations [34,35]. Most of the pressure measurements in the Von Karman swirl geometry were performed at the flow boundaries using piezoelectric transducers mounted through the wall of the cylindrical cell [34–37]. More recently, Dernoncourt *et al.* [42] have used ultrasound scattering technique to proceed to direct measurement of the vorticity in the bulk of the turbulent flow. By assisting pressure measurements with bubble visualization technique, Cadot *et al.* [34,35] have checked the direct correspondence between the recorded deepest pressure drops and the simultaneous observation of a filament passing by the point of measurement. In particular, these vorticity filaments were shown to be responsible for the deviation from a Gaussian distribution (observed on the high pressure side) of the (negative) low pressure tail of the pressure fluctuation histogram which displays a clear exponential dependence.

The role of vorticity filaments in fully developed turbulent flows is without any doubt, one of the very challenging issues that has received considerable interest during the past few years in the turbulence community [22–42]. As reported in references [34], these intense vortical structures are likely to play an important role in the dynamical structuration of the flow. The way they form, as well as the way they disappear *via* some vortex breakdown instability into smaller and thinner braided vortices (that are likely to correspond to the "worms" observed numerically by Jimenez *et al.* [27]), may be crucial mechanisms to account for the intermittency phenomenon [1–4]. Vorticity filaments are localized structures which clearly violate Kolmogorov 1941 (K41) hypothesis that assumes homogeneity and isotropy [48]. One may thus wonder whether they are at the origin of the experimental departure from K41 scaling observed when studying velocity fluctuation statistics [8]. In other words, one would be pleased to know up to which extend these vorticity filaments can be associated with intermittency. In previous experimental studies, vortex filaments were detected using standard thresholding technique on either pressure [34,35] or velocity derivative [41] measurements. This amounts to associate these filaments with the low pressure tail of the pressure fluctuation histogram or with the tails of the velocity derivative fluctuation histogram. The need of using a more reliable technique was raised by Abry *et al.* [37,38] who proposed to detect, characterize and remove the low pressure drops from the orthogonal wavelet decomposition of the experimental pressure signals. This more sophisticated method relies on the remark that large depressions have a characteristic pulse-like shape which involves a rather wide range of scales, a property which can be easily identified by the discrete wavelet transform; it just consists in looking at the time coincidence of large detail-coefficients on many different scales. In rather good agreement with the results of numerical simulations [27–29], it seems well established experimentally [34–39,42] that the length of the vorticity filaments corresponds to the largest scale of the flow namely the integral scale L, while their average core size is of the order of the Taylor microscale λ. Another very interesting experimental observation [34–37] is the fact that pressure drops scale like U^2, the square of the injection velocity, which indicates that the characteristic velocity increment on the core of the vortex is of the order of the integral velocity of the turbulent flow. As far as their statistical temporal distribution is concerned, the investigation of the probability density function (PDF) of the waiting time Δt between two successive vorticity filaments, reveals an exponential tail for large time intervals characteristic of a Poisson statistics [34,35,37,38]. For waiting times smaller than the turn-over time (*e.g.* the period of rotation of the disks in the Von Karman swirling flow experiments), the waiting time PDF decays algebraically which indicates that the depressions are no longer independent. Actually, as reported by Cadot *et al.* [34,35], the visualization shows that for short waiting times, the depressions are strongly correlated due mainly to two different reasons: (i) a filament can pass back and forth several times on the transducer; (ii) during vortex breakdown, the main filaments burst into several twisted and sometimes braided thinner (*i.e.* with a core size of the order of the Kolmogorov dissipation scale η) and shorter (*i.e.* with a characteristic length of the order of the Taylor microscale

λ) filaments that are likely to correspond to the "worms" observed numerically by Jimenez *et al.* [27]. Some preliminary attempts to investigate the statistical contribution of the vorticity filaments [37–39, 41, 49] have confirmed the numerical observation [27] that the effect of the elimination (from the statistics) of the filaments on the energy spectrum is somewhat negligible. But to our knowledge, there is no currently available quantitative estimation of the contribution of the vorticity filaments to intermittency [38, 39], *i.e.* to the observed experimental departure from K41 scaling [8].

The aim of the present work is to revisit previous analysis of pressure measurements in swirling turbulent flows [34–37] using the continuous wavelet transform (CWT) [50–63]. As compared to the orthogonal wavelet based approach developed by Abry *et al.* in reference [37], the CWT presents the crucial advantages of providing a continuous investigation of the range of scales available to the analysis and of being a representation that is invariant under time translation. As emphasized in early works [64–72], the CWT can be seen as a mathematical microscope which is well adapted for characterizing the scaling properties of fractal objects. In particular, the skeleton of the CWT defined by the wavelet transform modulus maxima (WTMM) [73, 74] was shown to contain all the information concerning the hierarchical distribution of the singularities of these objects. The so-called WTMM method introduced in references [75–81], provides a technical way of quantifying the relative statistical contributions of the singularities present in the data *via* the computation of the $D(h)$ singularity spectrum. This revisited multifractal formalism consists in investigating the scaling behavior of some partition functions defined on the WT skeleton. The key-point of the present study is that when focusing the CWT microscope on a strong depression, this pulse-like structure appears as a very strong singularity (*i.e.* a Dirac peak) when one continuously increases magnification from the integral scale down to the scale of the filament core below which the pressure signal is smooth [60, 82]. The maxima lines corresponding to these very strong "quasi" singularities are thus *a priori* easily distinguishable from the other maxima lines associated with weaker singularities characteristic of the background pressure fluctuations. Our goal is to define a protocol in order to identify in the WT skeleton, the set of maxima lines corresponding to the vorticity filaments. Then, by investigating systematically these maxima lines, one will be able to extract quantitative information on the structural characteristics of these filaments as well as on the way they are chronologically distributed. Furthermore, by applying the WTMM method on both the whole pressure WT skeleton and the "sub-skeleton" defined after removing the maxima lines corresponding to the filaments, one will be able to carry out a comparative multifractal analysis which will allow us to quantify the statistical contribution of the vorticity filaments to the so-called intermittency phenomenon.

The paper is organized as follows. In Section 2, we review some background material on the CWT [50–63]. We present the CWT as a mathematical microscope which is well suited for scanning the singularities of fractal functions [64–74]. We describe the WTMM method [75–81] as a natural generalization of box-counting algorithms [66, 83–85] and structure-function techniques [1–3] previously used for multifractal analysis of singular measures and multi-affine functions respectively. In Section 3, we apply the CWT to detect the presence of vorticity filaments in pressure measurements [60]. We calibrate the CWT based technique on stretched Burger vortex, a well accepted model for filaments [34, 35, 39, 41]. We define some criteria to select the WT maxima lines that correspond to vorticity filaments. We show also how to get information on the characteristic features of these localized structures from the behavior of the WT modulus along these maxima lines. We then apply our technique to experimental pressure data recorded by Couder and collaborators [33–35] in a Von Karman swirling flow experiment. We show that our methodology allows us to detect not only the deepest pressure drops associated with just formed rather straight filaments passing over the transducer but also some wider and more complex pressure drop patterns that are likely to be the signature of older filaments just after their breakdown. Section 4 is devoted to a quantitative analysis of the filament structural characteristics *via* a systematic investigation of the WT sub-skeleton defined by the maxima lines identified as corresponding to vorticity filaments. This sub-skeleton is further used to study the statistics of the waiting times between successive vorticity filaments. We comment on our results comparatively to the results obtained with different techniques in previously published works. In Section 5, we address the issue of the statistical contribution of the vorticity filaments to intermittency. We apply the WTMM method successively to the whole WT skeleton of the pressure data and to the sub-skeleton obtained once discarded the maxima lines corresponding to the filaments. On a more general ground, we discuss the actual relevance of the multifractal description of pressure fluctuations. We conclude in Section 6.

2 Singularity detection and processing with the wavelet transform modulus maxima

The continuous wavelet transform (CWT) is a mathematical technique introduced in signal analysis in the early eighties [50, 51]. Since then, it has been the subject of considerable theoretical developments and practical applications in a wide variety of fields [52–63]. The CWT has been early recognized as a mathematical microscope that is well adapted to reveal the hierarchy that governs the spatial distribution of the singularities of multifractal measures [62–72]. What makes the CWT of fundamental use in the present study is that its singularity scanning ability equally applies to singular functions than to singular measures [78–82].

2.1 The continuous wavelet transform

The CWT is a space-scale analysis which consists in expanding signals in terms of *wavelets* which are constructed from a single function, the *analyzing wavelet* ψ, by means of translations and dilations. The CWT of a real-valued function f is defined as [50,51]:

$$T_\psi[f](x_0,a) = \frac{1}{a}\int_{-\infty}^{+\infty} f(x)\psi(\frac{x-x_0}{a})dx \ , \qquad (3)$$

where x_0 is the space parameter and a (>0) the scale parameter. The analyzing wavelet ψ is generally chosen to be well localized in both space and frequency. Usually ψ is required to be of zero mean for the CWT to be invertible. But for the particular purpose of singularity tracking that is of interest here, we will further require ψ to be orthogonal to some low-order polynomials [64–69,78,79]:

$$\int_{-\infty}^{+\infty} x^m\psi(x)dx \ , \ \ \forall m \ , \ \ 0 \leq m < n_\psi \ . \qquad (4)$$

As originally pointed out by Mallat and collaborators [73, 74], for the specific purpose of analyzing the regularity of a function, one can get rid of the redundancy of the CWT by concentrating on the WT skeleton defined by its modulus maxima only. These maxima are defined, at each scale a, as the local maxima of $|T_\psi[f](x,a)|$ considered as a function of x. As illustrated in Figure 5b, these WTMM are disposed on connected curves in the space-scale (or time-scale) half-plane, called *maxima lines*. Let us define $\mathcal{L}(a_0)$ as the set of all the maxima lines that exist at the scale a_0 and which contain maxima at any scale $a \leq a_0$. An important feature of these maxima lines is that, wherever the analyzed signal displays scale invariance, there is at least one maxima line pointing towards the corresponding singularity from which one can estimate its strength [73–81].

2.2 Scanning singularities with the wavelet transform modulus maxima

The strength of a singularity of a function is usually defined by an exponent called *Hölder exponent*. The Hölder exponent $h(x_0)$ of a function f at the point x_0 is defined as the largest exponent such that there exists a polynomial $P_n(x)$ of order n satisfying [60–63]

$$|f(x) - P_n(x-x_0)| \leq C|x-x_0|^h \ , \qquad (5)$$

for x in a neighborhood of x_0. If $h(x_0) \in]n, n+1[$, one can easily prove that f is n times but not $n+1$ times differentiable at the point x_0. The polynomial $P_n(x)$ corresponds to the Taylor series of f around $x = x_0$, up to the order n. Thus $h(x_0)$ measures how irregular the function f is at the point x_0. The higher the exponent $h(x_0)$, the more regular the function.

This definition of the singularity strength naturally leads to a generalization of the so-called $f(\alpha)$ singularity spectrum introduced for fractal measures in references [86–88]. As originally defined by Parisi and Frisch [89], we will denote $D(h)$ the Hausdorff dimension of the set where the Hölder exponent is equal to h [78,79]:

$$D(h) = d_H\{x \ , \ h(x) = h\} \ , \qquad (6)$$

where h can take, *a priori*, positive as well as negative real values (*e.g.*, the Dirac distribution $\delta(x)$ corresponds to the Hölder exponent $h(0) = -1$).

Remark

The results reported in this work only apply to (fractal) functions whose singularities are not oscillating, *i.e.* satisfying $f' = df/dx$ is Hölder $h(x_0) - 1$ if f is Hölder $h(x_0)$. We refer the reader to references [90–92] for more details concerning oscillating singularities (chirps).

The main interest in using the CWT for analyzing the regularity of a function lies in its ability to be blind to polynomial behavior by an appropriate choice of the analyzing wavelet ψ. Indeed, let us assume that according to equation (5), f has, at the point x_0, a local scaling (Hölder) exponent $h(x_0)$; then one can easily prove that the local behavior of f is mirrored by the CWT which locally behaves like [74,93,94]:

$$T_\psi[f](x_0,a) \sim a^{h(x_0)} \ , a \to 0^+ \ , \qquad (7)$$

provided $n_\psi > h(x_0)$, where n_ψ is the number of vanishing moments of ψ (Eq. (4)). Therefore one can extract the exponent $h(x_0)$ as the slope of a log-log plot of the WT amplitude *versus* the scale a. On the contrary, if one chooses $n_\psi < h(x_0)$, then one can still prove that the WT behaves as a power-law but with a scaling exponent which is n_ψ:

$$T_\psi[f](x_0,a) \sim a^{n_\psi} \ , a \to 0^+ \ . \qquad (8)$$

Thus, around a given point x_0, the faster the WT decreases when the scale goes to zero, the more regular f is around that point. In particular, if $f \in C^\infty$ at x_0 ($h(x_0) = +\infty$), then the WT scaling exponent is given by n_ψ, *i.e.* a value which is dependent on the shape of the analyzing wavelet. According to this observation, one can hope to detect the points where $f \in C^\infty$ by just checking the scaling behavior of the WT when increasing the order n_ψ of the analyzing wavelet [76–79]. Let us also remark that if $h(x_0)$ is negative then the WT no longer decreases but instead increases when the scale a goes to zero; this remark will be of fundamental use in the next section for detecting vorticity filaments in pressure signals.

A very important (at least for practical purpose) point raised by Mallat and Hwang [74] is that the local scaling exponent $h(x_0)$ can be equally estimated by looking at the value of the WT modulus along a maxima line converging towards the point x_0. Indeed one can prove that both equations (7) and (8) still hold when following a maxima line from large scale down to small scale [74,77]. Thus the WTMM will be our key tool to study isolated singularities.

In Section 3, they will be at the heart of our strategy to recognize pressure drops associated to vorticity filaments from background pressure fluctuations.

The situation is somewhat more intricate when investigating fractal functions. Indeed the characteristic feature of these singular functions is the existence of a hierarchical distribution of singularities [64,75–81]. Locally, the Hölder exponent $h(x_0)$ is governed by the singularities which accumulate at x_0. This result in unavoidable oscillations around the expected power-law behavior of the WT amplitude [78–81,95]. Therefore the exact determination of h from log-log plots on a finite range of scales is somewhat uncertain [97,98]. Of course, there have been many attempts to circumvent these difficulties [81,98]. Nevertheless there exist fundamental limitations (which are not intrinsic to the WT technique) to the estimate of Hölder exponents of fractal functions. Consequently the determination of statistical quantities like the $D(h)$ singularity spectrum, requires a method which is more feasible and more appropriate than a systematic investigation of local scaling behavior of the WT. This is the purpose of the recently developed waveled-based multifractal formalism [75–81] that we will explicitly use in Section 5 to analyze the statistical scaling properties of the background pressure fluctuations.

2.3 A wavelet-based multifractal formalism: the wavelet transform modulus maxima method

A natural way of performing a multifractal analysis of fractal functions consists in generalizing the "classical" multifractal formalism [85–88] using wavelets instead of boxes. By taking advantage of the freedom in the choice of the "generalized oscillating boxes" that are the wavelets, one can hope to get rid of possible smooth behavior that could mask singularities or perturb the estimation of their strength h. But the major difficulty with respect to box-counting techniques [66,83–85] for singular measures, consists in defining a covering of the support of the singular part of the function with our set of wavelets of different sizes. A simple method would thus rely on the definition of the following *partition function* in terms of wavelet transform coefficients [64,78,79]:

$$Z(q,a) = \int |T_\psi[f](x,a)|^q dx \ , \qquad (9)$$

where $q \in \mathbb{R}$. This method based on a continuous covering of the real line would be a rather naive generalization of box-counting algorithms since nothing prevents the WT coefficients from vanishing at some point (x_0, a) of the space-scale half-plane. The partition function would then diverge for $q \leq -1$.

The wavelet transform modulus maxima (WTMM) method [75–81] implies that one changes the continuous sum over space in equation (9) into a discrete sum over the local maxima of $|T_\psi[f](x,a)|$ considered as a function of x:

$$Z(q,a) = \sum_{l \in \mathcal{L}(a)} |T_\psi[f](x,a)|^q \ . \qquad (10)$$

As emphasized in references [75,78,79], the branching structure of the WT skeleton in the (x,a) half-plane enlightens the hierarchical organization of the singularities. Thus the WT skeleton indicates how to position the oscillating boxes in order to obtain a partition of the singular behavior of f, at the considered scale a. Now from the deep analogy that links the multifractal formalism to thermodynamics [79,88], one can define the exponent $\tau(q)$ from the power-law behavior of the partition function:

$$Z(q,a) \ \sim \ a^{\tau(q)} \ , \ \ a \to 0^+ \ , \qquad (11)$$

where q and $\tau(q)$ play respectively the role of the inverse temperature and the free energy. The main result of this wavelet-based multifractal formalism is that in place of the energy and the entropy (*i.e.* the variables conjugated to q and τ), one has h, the Hölder exponent, and $D(h)$, the singularity spectrum. This means that the singularity spectrum of f can be determined from the Legendre transform of the partition function scaling exponent $\tau(q)$ [77,99]:

$$D(h) = \min_q (qh - \tau(q)) \ . \qquad (12)$$

From the properties of the Legendre transform, it is easy to see that *homogeneous* fractal functions that involve singularities of unique Hölder exponent $h = \partial\tau/\partial q$, are characterized by a $\tau(q)$ spectrum which is a *linear* function of q. On the contrary, a *nonlinear* $\tau(q)$ curve is the signature of nonhomogeneous functions that display *multifractal* properties, in the sense that the Hölder exponent $h(x)$ is a fluctuating quantity that depends upon the spatial position x.

As pointed out in references [78,79], one can avoid some practical difficulties that occur when directly performing the Legendre transform of $\tau(q)$, by first computing the following Boltzmann weights from the WT skeleton:

$$\hat{T}_\psi[f](q,l,a) = \frac{|T_\psi[f](x_l,a)|^q}{Z(q,a)} \ , \qquad (13)$$

where $Z(q,a)$ is the partition function defined in equation (10). Then one computes the following expectation values:

$$h(q,a) = \sum_{l \in \mathcal{L}(a)} \ln(|T_\psi[f](x_l,a)|)\hat{T}_\psi[f](q,l,a) \ , \qquad (14)$$

and

$$D(q,a) = \sum_{l \in \mathcal{L}(a)} \hat{T}_\psi[f](q,l,a) \ln(\hat{T}_\psi[f](q,l,a)) \ , \qquad (15)$$

whose slopes (*vs.* $\ln a$) provide estimates of $h(q)$ and $D(q)$ respectively and therefore of the $D(h)$ singularity spectrum.

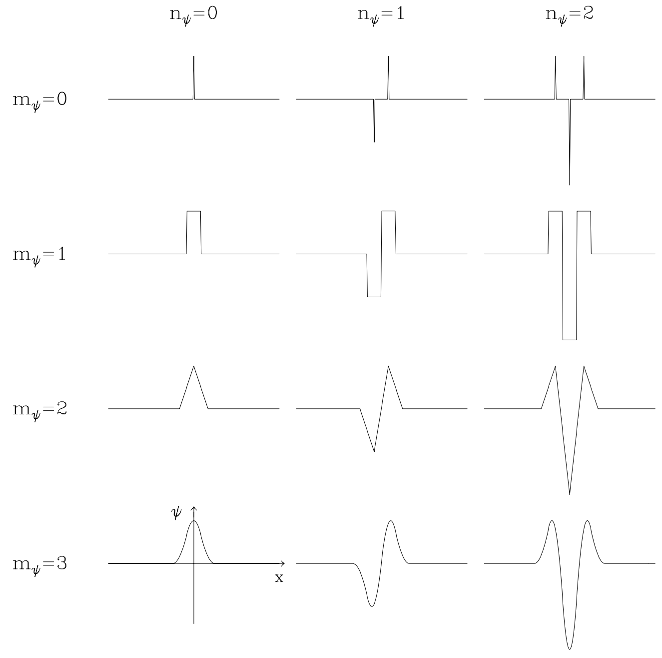

Fig. 1. Set of compactly supported analyzing wavelets $\psi_{(m)}^{(n)}$. n_ψ corresponds to the number of vanishing moments. The functions $\psi_{(m)}^{(n)}$ are smooth versions of $\psi_{(0)}^{(n)}$ obtained after m successive convolutions with the box function χ

The WTMM method has been tested on academic examples, *e.g.*, generalized devil's staircases and fractional Brownian motions [75–82]. It has already been successfully applied to numerical and experimental data from various domains such as fully developed turbulence [75,78,79,81, 82,100–102], DNA sequences [103–105], finance [106,107] and fractal growth phenomena [108,109].

2.4 Defining our battery of analyzing wavelets

There are almost as many analyzing wavelets as applications of the CWT. In previous works [65–72,75–81], we have mainly used the class of analyzing wavelets defined by the successive derivatives of the Gaussian function $G^{(N)}(x) = \frac{d^N}{dx^N} e^{-x^2/2}$ for which $n_\psi = N$. Throughout this study, we will rather use the set of compactly supported analyzing wavelets $\psi_{(m)}^{(n)}$ plotted in Figure 1 [82,100]. They are constructed from Dirac distributions ($\psi_{(0)}^{(n)}$) *via* successive convolutions with the box function χ. The index m_ψ, corresponding to the number of convolutions, characterizes the smoothness of the analyzing wavelet. n_ψ is by definition the number of vanishing moments of ψ.

Let us note that the functions $\psi_{(m)}^{(0)}$ are not analyzing wavelets since there are not of zero mean. However, when using $\psi_{(1)}^{(0)}$ (which is nothing else than the box function χ) into the (continuous) partition function defined in equation (9), one recovers classical box-counting techniques [66,83–85] commonly used for multifractal analysis of singular measures. Let us also remark that when using $\psi_{(0)}^{(1)}(x) = \delta(x-1) - \delta(x)$, the CWT is nothing but the local increment of the considered function and the (continuous) partition function (9) then reduces to the so-called structure function of order q [1–3]. We refer the reader to reference [76] where a comparative study of the structure function approach and the WTMM method is reported. Actually the structure function approach fails to fully capture the singularities present in a signal. The main insufficiencies of this method come from the irregular character of the analyzing wavelet $\psi_{(0)}^{(1)}$ and from the continuous integral used in equation (9). It is because the partition function in equation (10) is computed from the WT skeleton that the entire $D(h)$ singularity spectrum becomes accessible to the WTMM method. This is why the WTMM method is much more than a simple generalization of the box-counting techniques and the structure functions approach [75–82].

3 Detecting vorticity filaments with the wavelet transform modulus maxima

3.1 Description of the turbulent pressure data

In this paper, we study the experimental pressure signal recorded by Couder and his collaborators in a steady swirling turbulent flow in a 3D closed system [33–35]. The experimental setup is fully described in references [34,35]. The pressure time series has a very specific aspect as illustrated in Figure 2a where the pressure is expressed in units of standard deviations. Most of the time the signal exhibits random fluctuations around a mean value. These fluctuations are symmetrical and no difference is observed between the positive and negative fluctuations of small amplitude. However, large peaks are also observed intermittently in this signal. They are exclusively negative and correspond to depressions in the flow. In Figures 2b and 2c, the probability density function (PDF) of the values of the pressure signal is shown in linear and semi-logarithmic coordinates respectively. This PDF is extremely non symmetrical with the lowest negative pressure values that can be as small as 13 times the standard deviation while the highest pressure values do not exceed 5 times the standard deviation. Moreover, whereas the PDF on the positive side is well fitted by a Gaussian shape [33–35], its tail for negative pressures rather behaves as an exponential [33–37].

When using their bubble visualization technique, Couder *et al.* [30–35] have shown that each strong negative peak in the pressure signal corresponds to a filament passing on the transducer; reciprocally, all the filaments passing over the transducer are likely to induce a deep drop in the pressure signal. They have also brought evidence that the shape of the pressure drops corresponding to a filament passing directly on the probe, reflects the state of the filament. If the filament has just formed and is still straight, the pressure drop in the time series is deep and narrow (see Figs. 5a and 6a). Older filaments disappear through what appears to be a vortex breakdown process: the filament bursts into several smaller braided

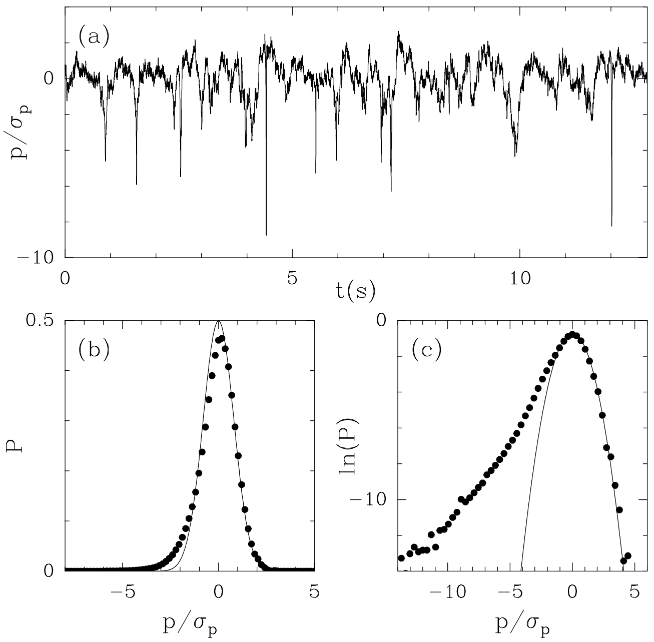

Fig. 2. (a) Time series of the pressure fluctuations over about 40 experimental turn over times (T). Pressure is expressed in units of standard deviations. The signal shows the superposition of symmetrical random background fluctuations with intermittent large amplitude depressions. PDF of the pressure values as shown in (b) linear coordinates and (c) semi-logarithmic coordinates. The positive side of this PDF is well fitted by a Gaussian shape (continuous line), while the tail on the negative side appears to be exponential.

strands which finally vanish. When this complex structure passes on the probe, the overall depression is still deep but is now broader and presents multiple secondary negative peaks (see Fig. 7a). Without visualization, one can assume that a deep and narrow negative peak systematically corresponds to a young filament passing on the transducer. On the other hand, a broader peak or a peak with complex structure doesn't correspond necessarily to a burst filament. Indeed the width of the pressure drops depends on the advection velocity of the filaments which can take values between $-\Omega R$ and ΩR where $\pm\Omega/2\pi$ are the rotation frequencies of the two contra-rotating disks and R their radius. So the temporal width detected by pressure measurement doesn't directly give access to the spatial size of the depression. In rare cases, a filament can inverse its advection velocity and pass several times on the transducer. Then several consecutive narrowly spaced depression peaks are recorded. However, when some complex low pressure structure is observed, it is likely to correspond to a burst filament. Another interesting experimental observation is that a filament takes less space and lives a shorter time in its concentrated state than in its burst state. Consequently the probability to have a filament on the transducer is less important for a young filament than for a burst one. Actually most of the deep pressure drops that are recorded have a complex structure that requires a specific detection technique to be recognized as corresponding to a vorticity filament.

3.2 Wavelet based characterization of Burgers vortex

In previous works [34,35,39,41], the Burgers vortex (which is a stationary solution of the incompressible 3D Navier-Stokes equations (NS)) has been emphasized as a well accepted model for the young filaments corresponding to deep and narrow depressions in the recorded pressure signals. In this model, the velocity field is defined in cylindrical coordinates by:

$$\begin{cases} u_r = -\frac{1}{2}\gamma r \ , \\ u_\phi = \frac{\Gamma}{2\pi r}(1 - e^{-r^2/4r_0^2}) \ , \\ u_z = \gamma z \ , \end{cases} \tag{16}$$

where $r_0 = \sqrt{\nu/\gamma}$ is the core radius and Γ the circulation of the vortex. This circulation is linked to the maximal rotation velocity (also called peripheral velocity), $\Gamma = 2\pi r_0 u_\phi^{max}/0.32 = 2\pi r_0 u_0$. By replacing in the NS equations, the velocity field by the expression given in equation (16), one obtains after integration:

$$p(r,\phi,z) - p(0,\phi,0) = -\frac{1}{2}\rho\gamma^2(r^2 + \frac{z^2}{4}) + \rho\frac{\Gamma^2}{4\pi^2}\int_0^r \frac{(1 - e^{-(x/2r_0)^2})^2}{x^3}dx \ . \tag{17}$$

In the particular case where the stretching is negligible as compared to the rotation or when the vortex is no longer stretched, one can approximate $u_r \sim u_z \sim 0$ and the pressure field is then given by the integral form:

$$p(r/r_0) = \rho\frac{\Gamma^2}{4\pi^2 r_0^2}\int_{-\infty}^{r/r_0} \frac{(1 - e^{-(x/2)^2})^2}{x^3}dx \ . \tag{18}$$

Although in reality the filaments are certainly less axisymmetrical than the ideal Burgers vortex shape defined in equation (16), the coincidences observed with the bubble visualization techniques [34,35] show that the recorded depressions actually correspond to filaments perpendicular to the wall (where the piezoelectric transducer is located) and generally situated in the main shear layer. Moreover, all the filaments do not pass exactly on the transducer and their incident velocity angle with respect to the probe axis fluctuates about some mean value which is not too different from $\pi/2$ (the probe surface is tangential to the inner surface of the wall and since the measurements are performed in the main shear layer, the advection velocity of the filaments is in good approximation tangential to the wall). We refer the reader to references [39,41], where the influence of various geometrical parameters (*e.g.*, the angle of the vortex axis with respect to the probe axis, its incident angle and the distance at which it passes from the probe) on the shape of the velocity field of a Burgers vortex has been discussed and further used to interpret experimental data.

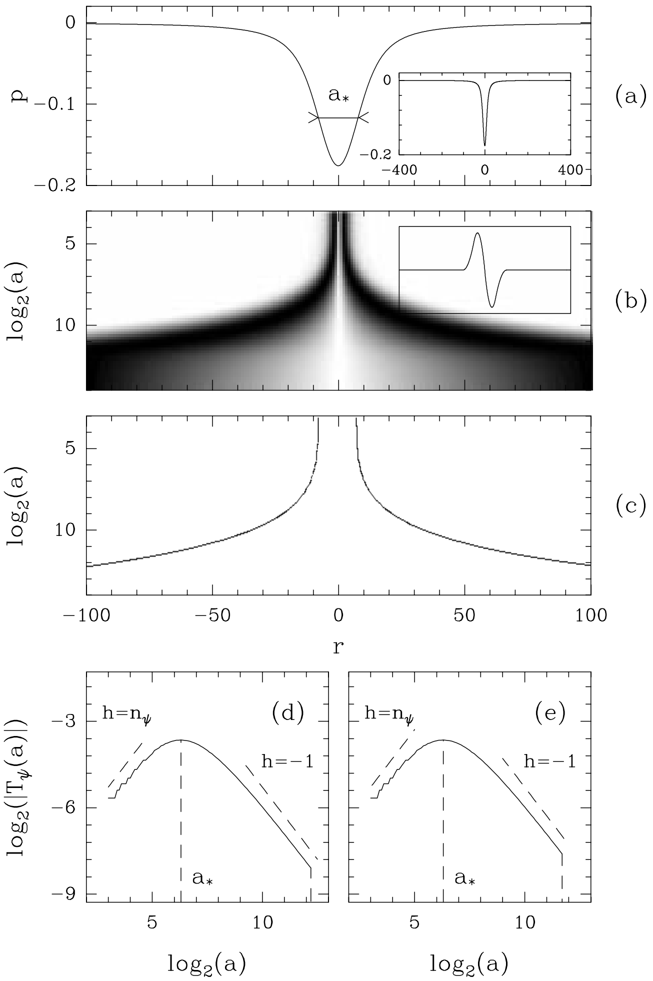

Fig. 3. WT of the pressure field of a Burgers vortex. (a) Profile of the pressure given by equation (18) with $u_0 = 1$ and $r_0 = 10$. (b) WT of this signal computed with the analyzing wavelet $\psi^{(1)}_{(3)}$; the amplitude is coded, independently at each scale a, using 32 grey levels from white ($|T_\psi[p](x,a)| = 0$) to black ($\max_x(|T_\psi[p](x,a)|)$). (c) WT skeleton defined by the set of WTMM lines. (d) and (e) show the behavior of the wavelet coefficients along the left and right maxima lines respectively. The scale a_* corresponds to the scale shown in (a).

The pressure field given by equation (18) is illustrated in Figure 3a when considering the parameter values $u_0 = 1$ and $r_0 = 10$, and when imposing the pressure to be zero at infinity as a reference value. Let us note that the minimum pressure is linked to the peripheral velocity by the relation: $p_{min} = -1.69(u_\phi^{max})^2 = -0.173u_0^2$. On the other hand, the characteristic width of this depression is equal to r_0. In Figures 3b and 3c, we present respectively the WT of this Burgers vortex pressure signal and its WT skeleton computed with the analyzing wavelet $\psi^{(1)}_{(3)}$ (Fig. 1) [82]. This skeleton is made of two maxima lines which point to the depression. The behavior of the wavelet coefficients along these maxima lines is shown in Figures 3d and 3e, for the left and right lines respectively. The WT modulus increases when decreasing a with a power-law behavior with exponent $h = -1$ (Eq. (7)), down to some scale a_*. For scales $a < a_*$, the WT modulus no longer increases but behaves with a power-law exponent $n_\psi = 1$, where n_ψ is the number of null moments of the considered analyzing wavelet (Eq. (8)). Let us point out that the wavelet coefficients behave in the same way on the two maxima lines except that the coefficients are positive on one maxima line and negative on the other one. So the space-scale analysis of the pressure Burgers vortex provided by the WT skeleton reveals the following main characteristic behavior:

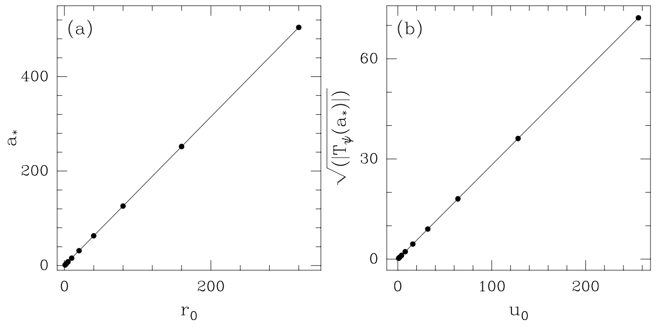

Fig. 4. Calibrating our wavelet-based methodology on Burgers vortex: study of the behavior of a_* and $|T_\psi(a_*)|$ as a function of the characteristic parameters of the Burgers vortex. (a) a_* *vs.* r_0: the continuous line obtained by linear regression fit has a slope equal to 1.58 and a null intercept (Eq. (19)). (b) $\sqrt{|T_\psi(a_*)|}$ *vs.* u_0: the continuous line has a slope equal to 0.28 and a null intercept (Eq. (20)). The analyzing wavelet is $\psi^{(1)}_{(3)}$.

- At large scale: $a > a_*$, this vortex can be assimilated to a Dirac distribution which corresponds to a strong singularity of (Hölder) exponent $h = -1$.
- At small scale: $a < a_*$, the WT microscope actually explores the vortex core which is in fact a smooth function. According to equation (8), the exponent obtained is the number of null moments of the analyzing wavelet (here, $n_\psi = 1$).

The scale a_* is linked to the width at mid-height of the vortex core. We can easily demonstrate that a_* is linearly dependent on the parameter r_0, the characteristic width of the vortex. As shown in Figure 4a, the values obtained for a_* as a function of r_0 systematically fall on a straight line of slope 1.58:

$$a_* = 1.58 r_0 \ . \tag{19}$$

Likewise the maximum WTMM at scale a_*, $|T_\psi(a_*)|$, is linked to the depth of the vortex and then to the square of u_0. When plotting in Figure 4b, the square root of $|T_\psi(a_*)|$ as a function of the parameter u_0, we otain a well defined straight line of slope 0.28:

$$|T_\psi(a_*)|^{1/2} = 0.28 u_0 \ . \tag{20}$$

Through the relationships (19, 20), the WTMM allow us to estimate the characteristic parameters of the Burgers

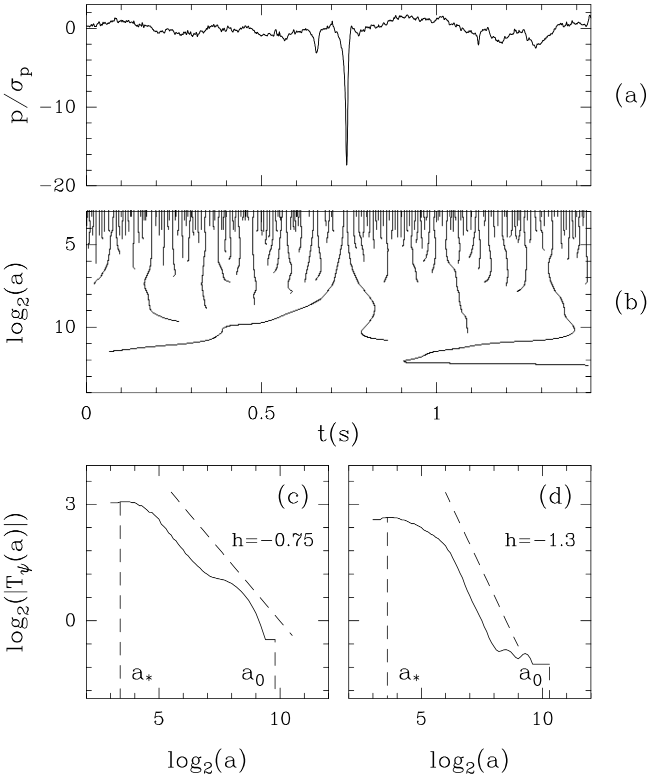

Fig. 5. Time-scale analysis of a sample of the pressure signal containing a deep depression due to a young filament passing over the transducer. (a) Time series of the pressure fluctuations. (b) WT skeleton computed with the analyzing wavelet $\psi^{(1)}_{(3)}$. (c) and (d) show the behavior of the WT modulus along the two maxima lines which point to the filament position as a function of the scale parameter a in logarithmic coordinates. The power-law increase of the WT modulus observed when decreasing a, down to some small inner scale a_*, is quite similar to the behavior obtained for Burgers vortex in Figures 3d and 3e.

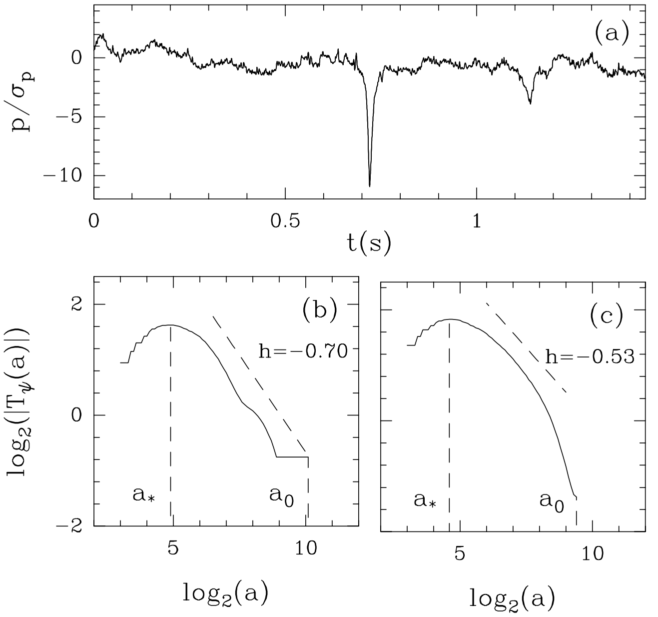

Fig. 6. (a) Pressure signal containing a young filament. (b) and (c) illustrate the behavior of the WT modulus along the two maxima lines which point to the filament position as a function of the scale parameter a in logarithmic coordinates. The analyzing wavelet is $\psi^{(1)}_{(3)}$.

vortex, namely r_0 and u_0. Let us point out that similar linear dependence is found when using analyzing wavelets of higher order [82]; the only difference comes from the value of the slopes (respectively 1.58 and 0.28) in equations (19, 20) which are naturally wavelet dependent.

The WT skeleton therefore provides a very efficient way to detect vortical structures. From the characteristic behavior of the WTMM along the maxima lines one can estimate the geometrical characteristics of these filaments directly from the experimental pressure signal without using arbitrary thresholding technique on the signal amplitude [60,82].

Remark

The pressure of a Burgers vortex defined in equation (18) is a C^∞ function. The Hölder exponent of this function is thus $h(0) = +\infty$ at $x_0 = 0$ where is located the vortex. Nevertheless, the fact that at scales $a > a_*$, this depression can be assimilated to a localized peak, makes sound the identification of these particular events to strong ($h(0) = -1$) "quasi" singularities of the pressure field.

3.3 Detecting vorticity filaments with the wavelet transform modulus maxima

3.3.1 Young filaments

We have detected by a simple thresholding technique a lot of young filaments for which we have studied the behavior of the WTMM [82]. In Figure 5a, we present a sample of the pressure signal which contains a young filament with an amplitude drop of about $-20\sigma_p$. The WT skeleton of this signal, as computed with the analyzing wavelet $\psi^{(1)}_{(3)}$, is shown in Figure 5b. Let us point out that the crossing of the filament over the probe seems to erase all the surrounding fluctuations as observed on the WT skeleton which doesn't display any maxima line in the neighbourhood of the two lines corresponding to the filament itself (this phenomenon is also visible on the previous "little" filament). In Figures 5c and 5d, the WT modulus along these two maxima lines is plotted as a function of the scale parameter a in logarithmic coordinates. The corresponding curves clearly increase from a large scale a_0 where the maxima lines appear, down to a very small scale a_* which is found almost identical for the two lines. At large scale, for $a > a_*$, one thus recovers the characteristic behavior of a strong singularity of negative Hölder exponent $h \simeq -1$, as previously observed for Burgers vortex (Figs. 3d and 3e). Let us note that for this particular very intense depression, the smallness of a_* prevents us from exploring the smoothness of the filament core at scales $a < a_*$. As illustrated in Figure 6, we have reproduced this WTMM scaling analysis for different recorded depressions of amplitude deeper than $-10\sigma_p$. This systematic study of the young filaments brings the clue that this "abnormal" increase of the WT modulus when decreasing a is always verified. Moreover the fact that the scale a_* does not depend upon the considered maxima line seems to be a robust feature from which one can extract the temporal width of the depression (Eq. (19)) with a high degree of confidence. As shown in Figures 6b and 6c, when the characteristic inner scale a_* is not too small, one can check that for scales $a < a_*$ the WT modulus decreases when further decreasing a. Unfortunately, because of the low sampling rate as compared to the filament width, the range of scales left to scaling analysis is so tiny that it is hopeless to check accurately the validity of equation (8). Nevertheless, the fact that this decrease is found to be very sensitive to the order of the considered analyzing wavelet, can be seen as a strong indication that when increasing enough the magnification of the WT microscope, one ultimately explores the filament core and reveals its smoothness. Furthermore, let us mention that we have verified that, as predicted for Burgers vortex (Eq. (20)), $|T_\psi(a_*)|$ is proportional to the depth of the pressure drop [82].

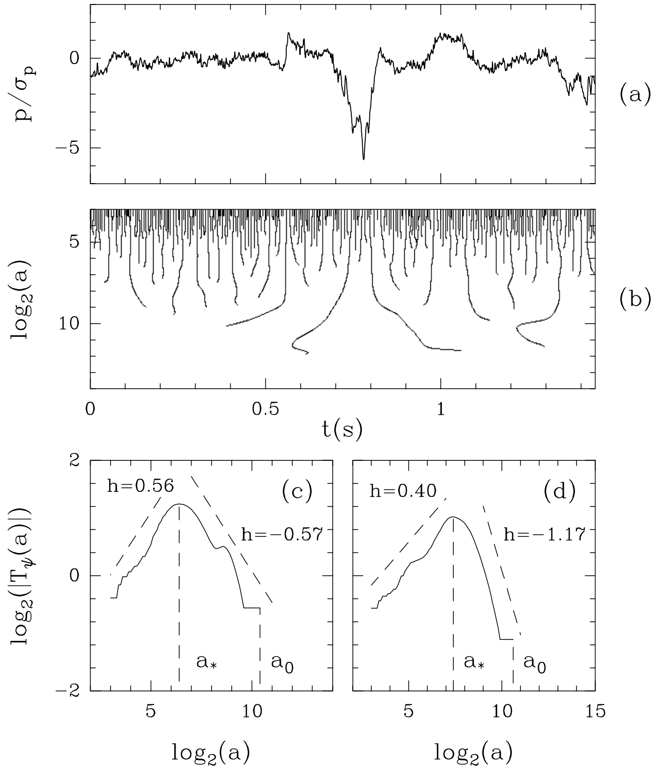

Fig. 7. Time-scale analysis of a sample of the pressure signal illustrating the effect on pressure fluctuations of a burst filament passing over the transducer. (a) Time series of the pressure fluctuations. (b) WT skeleton computed with the analyzing wavelet $\psi^{(1)}_{(3)}$. This skeleton contains maxima lines inside the core of the filament which enlightens the inner complexity of this structure. (c) and (d) illustrate the behavior of the WT modulus along the two maxima lines which point respectively to the large drop and large jump that delimit the extend of the filament. These results are qualitatively similar to those obtained for the Burgers vortex in Figures 3d and 3e, except that the inner scale a_* is different for the two maxima lines and that the core of the filament is larger and no longer smooth.

3.3.2 Burst filaments

In the same way, we have detected different filaments with a complex internal structure, that we will call burst filaments [82]. In Figure 7, we present one of these filaments (Fig. 7a) together with its WT skeleton (Fig. 7b). Note that this skeleton shows maxima lines around the filament as well as in between the two maxima lines which point to the two great jumps which delimit (to the right and to the left) the extend of the core of this burst filament. The behavior of the wavelet coefficients along these two maxima lines is represented in Figures 7c and 7d. It is qualitatively very similar to the behavior observed for the young filaments except that the characteristic inner scale a_* is significantly larger as reported before. For scales $a > a_*$, the WT modulus increases when the scale is decreased as the signature of a strong singularity with negative Hölder exponent. For scales $a < a_*$, the WT modulus follows an approximate power-law with an exponent clearly smaller than n_ψ. Let us point out that the range of scales left below a_* is now large enough to allow the estimate of a scaling exponent. For the filament shown in Figure 7, we obtain from linear regression fit in Figures 7c and 7d, the values $h \simeq 0.57$ and $h \simeq 0.4$ for the left and right maxima lines respectively. Similar quantitative results are obtained when considering different analyzing wavelets of higher order. Indeed the core of the filament is no longer smooth but displays some roughness properties that are comparable to those of the background pressure fluctuations characterized by a finite range of positive singularity exponents (Section 5.1). Note that on the contrary to the young filaments with a well defined smooth core, the burst filaments have a more complex inner structure delimited by two maxima lines in the WT skeleton along which the WT modulus reaches its maximum at a scale a_* which is no longer the same for these two lines. This asymmetry makes the use of equation (19) derived for Burgers vortex quite questionable. In Section 4.2, we will proceed to a statistical study of the filament core size including young and burst filaments. For the latter we will approximate the width of their core by putting in the left-hand side of equation (19), the arithmetic mean value of the scales a_* measured on the left and right maxima lines; the width of the burst filaments so obtained will thus correspond to the core size of some "average" axisymmetrical Burgers like young filaments. As illustrated in Figure 8 for a different burst filament, the quantitative features observed on the WTMM in Figure 7 are likely to be robust characteristic features that can be used to differentiate rather old burst filaments from just formed Burgers like filaments [82].

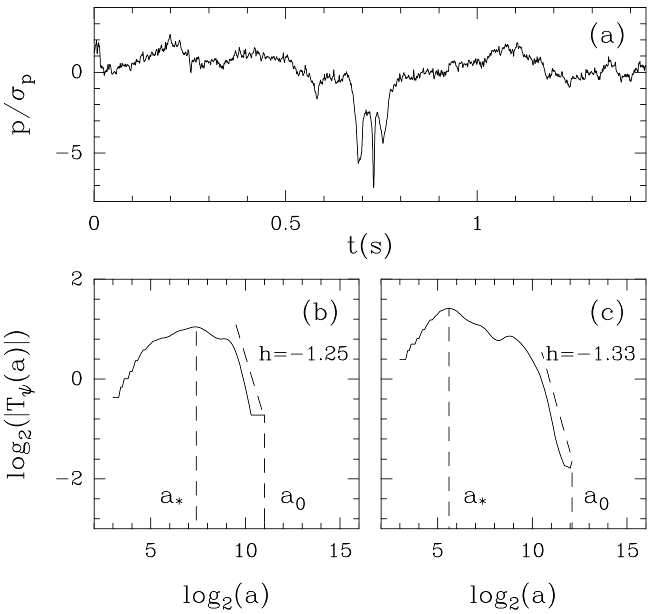

Fig. 8. (a) Pressure signal containing a burst filament. (b) and (c) illustrate the behavior of the WT modulus along the two maxima lines which delimit the extend of the filament, as a function of the scale parameter a in logarithmic coordinates. The analyzing wavelet is $\psi_{(3)}^{(1)}$.

3.4 Discriminating vorticity filaments from background pressure fluctuations

From the results reported in the previous section, one can reasonably hope to resort to the WT and to the restriction to its modulus maxima, to distinguish a filament passing on the transducer from the background pressure fluctuations that are likely to be symmetrical [60,82]. For each maxima line, we simply have to record the scale a_0 where the maxima line appears, and to find the maximum of $|T_\psi[p](a)|$ when going down the scales along this maxima line. We thus obtain a_* and $|T_\psi(a_*)|$. If $a_* = a_0$, this maxima line corresponds to a weak singularity certainly due to symmetrical fluctuations. Conversely, if a_* is significantly smaller than a_0, this line is likely to correspond to a strong singularity and thus to a filament. However, when applying these criteria to analyze fractional Brownian motions [110,111] of parameter $H = 2/3$ (*i.e.* a stochastic signal which has a $k^{-7/3}$ power spectrum like the pressure data of interest here [34,35]), one finds that a lot af maxima lines exist for which a_* is different from a_0. Therefore we need a more efficient criterion than simply $a_* \neq a_0$ to distinguish the filaments from background fluctuations. In Figure 9, we show the results of a comparative statistical study of the WT maxima line characteristics of the fractional Brownian signal of parameter $H = 2/3$ (with the same standard deviation as the experimental pressure signal) and of the experimental pressure signal. For the fractional Brownian signal, the data points obtained when plotting $\log_2(|T_\psi(a_*)|)$ *versus* $\log_2(a_*)$ in Figure 9a, form a cloud of mean slope close to $H = 2/3$ (dashed line).

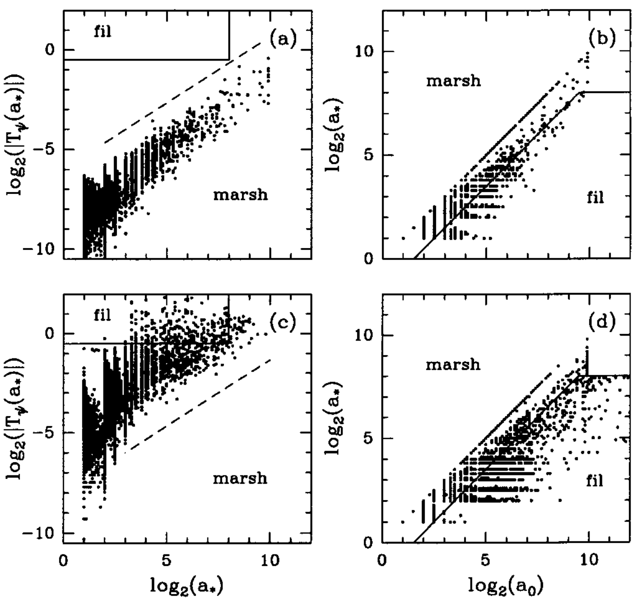

Fig. 9. Comparative statistical analysis of the characteristics of the WT maxima lines of a fractional Brownian signal of parameter $H = 2/3$ and of the experimental pressure signal. The standard deviation of both these signals was fixed to 1. Fractional Brownian signal: (a) $\log_2(|T_\psi(a_*)|)$ *vs.* $\log_2(a_*)$; (b) $\log_2(a_*)$ *vs.* $\log_2(a_0)$. Pressure signal: (c) $\log_2(|T_\psi(a_*)|)$ *vs.* $\log_2(a_*)$; (d) $\log_2(a_*)$ *vs.* $\log_2(a_0)$. The dashed lines in (a) and (c) correspond to a slope $H = 2/3$. The continuous lines delimit the separation between the "filament phase" and the "background pressure fluctuations phase" according to the criteria defined in equation (21). The analyzing wavelet is $\psi_{(3)}^{(1)}$.

Comparatively, the cloud obtained for the pressure signal in Figure 9c is broader and more diffuse while for a same value of a_*, the values of $|T_\psi(a_*)|$ are more important. In fact this observation shows the existence of very intense events in the pressure data. In Figures 9b and 9d, a_* is plotted as a function of a_0 for both the numerical and experimental signals using logarithmic coordinates. For the fractional Brownian signal, 82% of the maxima lines have a_* equal to a_0 as compared to only 55% for the pressure signal. Moreover, for a same value of a_0, a_* takes smaller values for the pressure signal which means that over a wide range of scales the WT modulus increases (instead of decreasing) when the scale parameter a is decreased. Let us point out that the total number of maxima lines obtained for the fractional Brownian signal is about twice as large as the total number obtained for the pressure signal. This is possibly a consequence of the presence of filaments in the pressure signal which erase fluctuations in their neighbourhood as shown in Figure 5b.

Along the line of these observations, we have carried out a systematic study of the WT skeleton of the experimental pressure signal with the specific goal to define criteria which will allow us to identify young as well as burst filaments. In the remainder of this paper, we will consider that a maxima line corresponds to a filament if the three

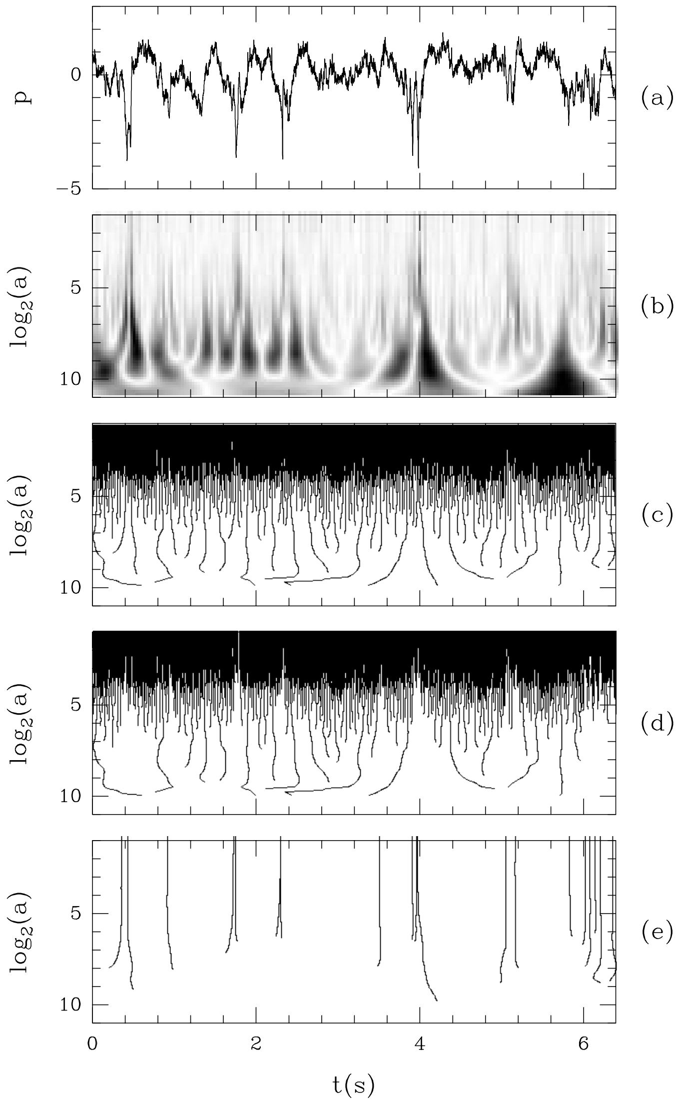

Fig. 10. (a) A sample of the pressure signal. (b) WT of the pressure signal; the amplitude is coded independently at each scale a, with 32 grey levels from white ($|T_\psi(t,a)| = 0$) to black ($\max_t(T_\psi(t,a))$. (c) WT skeleton of the pressure signal. (d) Sub-skeleton corresponding to the symmetrical background pressure fluctuations. (e) Complementary sub-skeleton involving only maxima lines which verify conditions (21); this sub-skeleton corresponds to the "filament phase". The analyzing wavelet is $\psi_{(3)}^{(1)}$.

conditions listed below are fulfilled [82]:

$$\begin{cases} \bullet\ \log_2(a_0/a_*) > 1.5\ ; \\ \bullet\ \log_2(|T_\psi(a_*)|) > -0.5\ ; \\ \bullet\ \log_2 a_* < 8\ . \end{cases} \tag{21}$$

The first condition results from the necessity of checking that on a finite range of scales ($[a_*, a_0]$), the filaments can be assimilated to a Dirac peak. The second condition amounts to some thresholding on the pressure amplitude; it is necessary in order to avoid assimilating as filaments an important number of maxima lines which appear at small scale ($a_0 < 2^5$) and which correspond to rather small pressure drops. Indeed we are not sure that these peaks result from the presence of a filament because they are also observed on the fractional Brownian signal. Let us note that if one uses equation (20) together with the previously mentioned relationship $p_{min} = -0.173u_0^2$ derived for Burgers vortex, this second condition does not appear to be very stringent since it consists in discarding pressure drops of amplitude smaller than $|p_{min}| < \sqrt{2}\sigma_p$ only. The third condition has been added in order to avoid to take into account rather large variations of the signal amplitude over a time interval of the order of one turn-over time $T = 2\pi/\Omega$ ($\log_2 T = 9.5$) and which doesn't correspond to a filament passing over the probe. When these three conditions are verified, we detect with a rather good precision nearly all the filaments that can be identified by the bubble visualization technique and many others that would have been missed when using a rather crude thresholding technique as experienced in previous works to detect the young filaments [33–35,41].

The different stages of our strategy for discriminating vorticity filaments from background pressure fluctuations are illustrated in Figure 10 [60,82]. Figures 10a and 10b show a sample of the pressure signal together with its WT coded, independently at each scale a, with 32 grey levels and computed with the analyzing wavelet $\psi_{(3)}^{(1)}$. The corresponding WT skeleton is presented in Figure 10c. For each maxima line, we determine the quantities a_0, a_* and $T_\psi(a_*)$. Then we classify these lines into two categories corresponding to two different "phases" of pressure fluctuations. In Figure 10d, we extract the WT sub-skeleton associated with the symmetrical background pressure fluctuations, *i.e.* the set of maxima lines which do not verify the conditions (21). The complementary of this sub-skeleton is shown in Figure 10e; it corresponds to the "filament" phase. All the maxima lines point to a pressure drop (or jump) characteristics of a filament passing over the transducer. Let us point out that we detect non only the deepest depressions associated to young filaments and which can be equally detected using simple thresholding technique, but also the pressure drops and jumps corresponding to burst filaments. In Section 4, we will mainly concentrate our study on the WT sub-skeleton corresponding to the filament contribution. From a systematic investigation of this sub-skeleton, we will carry out a statistical analysis of the filament structural properties and of their temporal distribution. In Section 5, we will apply the WTMM method [75–82] to the WT sub-skeleton corresponding to the background pressure fluctuations, with the specific goal to determine quantitatively the actual contribution of the vorticity filaments to the multifractal properties of the pressure fluctuations.

4 Statistical analysis of the vorticity filaments using the wavelet transform modulus maxima

This section is devoted to a statistical analysis of the vorticity filaments as detected from the experimental pressure signal using the wavelet-based criteria (21) established in the previous section. For comparison, we will also present the results obtained with a less accurate identification test which will consist in simply selecting the WT maxima lines which verify the condition $a_* \neq a_0$. As explained before, with this less stringent condition, we are certain to detect all the filaments but we are also aware that among the retained maxima lines, some of them actually correspond to background pressure fluctuations and not to vorticity filaments passing over the probe.

4.1 Advection velocity of the vorticity filaments

As discussed in Section 3, the characteristic scale a_* computed from the WT maxima lines that are identified as corresponding to a filament, is directly linked to the size of the filament core. Nevertheless, what is actually measured is a temporal width which corresponds to the time taken by the filament to cross over the transducer. A reasonable (at least for the young filaments) definition of the spatial width of these filaments is given by the following formula:

$$r_0 = r_0(a_*)|U^f_{adv}| \, , \tag{22}$$

where $r_0(a_*) = a_*/1.58$ is the characteristic inner time scale of a static Burgers vortex associated to the scale a_* (Fig. 4a), while U^f_{adv} is the advection velocity of the recorded filament. To determine this velocity, we must know the component of the velocity field parallel to the wall. In reference [34,35], Couder *et al.* devised an experimental set up to measure simultaneously this velocity and the pressure field. This apparatus involved three detectors with a particular disposition: the two pressure probes are placed in the wall, half way between the stirrers and horizontally separated by a distance $d = 1\,\text{cm}$; the hot wire probe is placed between the two pressure probes and perpendicular to the wall in order to measure $U_{//}$. In Figures 11a and 11b are shown a sample of both the pressure and velocity signals recorded simultaneously by one of the transducers and the hot wire. The velocity signal presents sudden fall downs towards zero. These particular events are a direct consequence of the fact that the hot wire actually measures the absolute value of $U_{//}$ and not $U_{//}$ itself. Since the measurement is made in the turbulent shear layer, *i.e.* in a region where $U_{//}$ often changes its sign ($\langle U_{//}\rangle = 0$ in this region), $|U_{//}|$ is expected to exhibit some drops to zero each time there is a change of sign of $U_{//}$. Let us point out that on the contrary to what is observed on the pressure signal, it is rather difficult to identify on the velocity signal, the signature of special events associated to a filament crossing the hot wire.

Remark

We saw in Section 3 that each filament is detected by two WT maxima lines when we use the analyzing wavelets $\psi^{(1)}_{(n)}$ which have only one zero moment. The wavelet coefficients are positive on one line and negative on the other one. In the following of this section, we will restrict our study to the maxima lines such that $T_\psi(a_*) < 0$. Similar results are obtained when retaining alternatively the lines such that $T_\psi(a_*) > 0$.

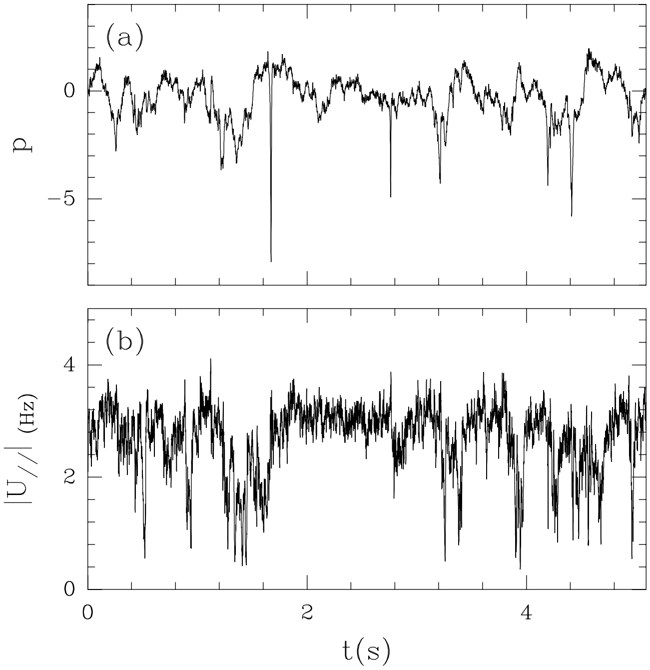

Fig. 11. Simultaneous recording of (a) pressure and (b) longitudinal velocity. The sudden fall downs towards 0 of $|U_{//}|$ come from the intermittent changes of the velocity sign.

Now comes the question of computing the advection velocity of the filaments from the recorded velocity signal. One possibility would be to use the complementary information coming from the two pressure probes. For example one could detect on the two pressure signals, the positions t_1 and t_2 where the maxima lines point to the same filament passing successively over the two probes. The advection velocity could then be computed from the relation $|U^f_{adv}| = d/|t_2 - t_1|$, or by averaging the recorded velocity $|U^f_{adv}| \approx \frac{1}{|t_2-t_1|}\int_{t_1}^{t_2} |U_{//}(t)|dt$. But this method, based on the detection of a same event by two different transducers, is difficult to calibrate: indeed a filament can evolve from both a structural and a dynamical point of view in between its successive passings over the two transducers. Moreover a filament doesn't always pass along the axis that joints the two transducers and sometimes can even be detected by one transducer only. In this case, the so-obtained velocity may not correspond to the advection velocity of the filament and its spatial core size may be dramatically underestimated. A more reliable method actually consists in using the information coming from one pressure probe only and more specifically from the time-scale representation provided by the WT of the recorded pressure signal. The scale a_*, determined for each filament from the WTMM, being proportional to the temporal width of its core, one can then estimate the filament advection velocity from the following averaging formula [82]:

$$U_{adv}^{f} = \frac{1}{a_*}\int_{t_1-a_*/2}^{t_1+a_*/2} |U_{//}(t)|dt, \qquad (23)$$

where t_1 is the time identified from the WT skeleton as the passing time of the filament over the first transducer.

In Figure 12a are reported the PDFs of the filament advection velocity obtained when considering two different selection criteria for the filaments, namely when using all the maxima lines that verify $a_* \neq a_0$ (○) or when considering only those that fulfill equation (21) (●). The former distribution is slightly shifted towards larger values of $|U_{adv}^{f}|$ as compared to the PDF obtained for the recorded ($|U_{//}|$) velocity signal (continuous line). This effect is probably due to the fact that we take into account (additional) maxima lines that do not correspond to a filament and for which the estimated value of a_* is very small. On the other hand, the PDF obtained from the maxima lines which verify our filament selection criteria (Eq. (21)) is maximum for a value which is very close to the integral velocity ΩR of the rotating disks, and looks very much like the PDF of $|U_{//}|$. A different look at the differences between these three PDFs is given in Figure 12b when using a semi-log representation. It appears clearly that the PDF of the filament advection velocity estimated using equations (21, 23), decreases more quickly for the small values of $|U_{//}|$ than the two other PDFs which admit values close to zero. This result is rather intuitive since the probability to detect (on the two transducers as well as on the hot wire) a filament with an advection velocity close to zero is very small.

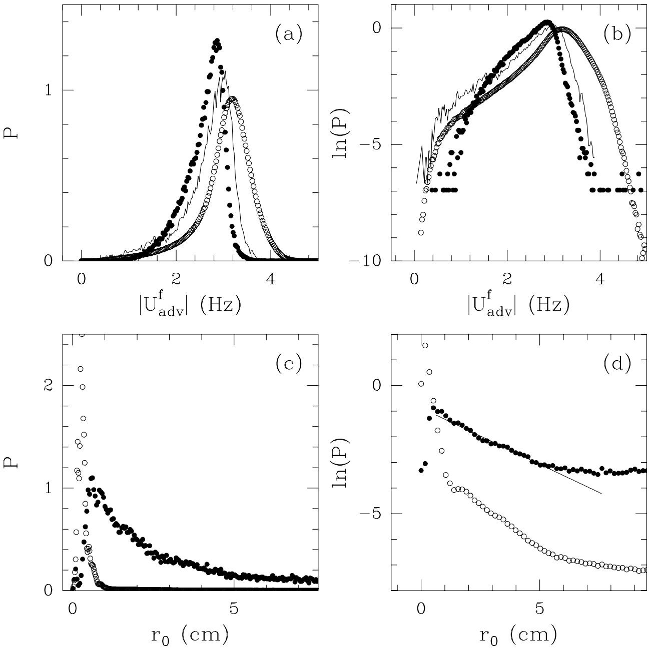

Fig. 12. (a) PDFs of the advection velocity $|U_{adv}^{f}|$ computed from the maxima lines which verify respectively $a_* \neq a_0$ (○) and conditions (21) (●). The continuous line corresponds to the PDF of $|U_{//}|$. (b) Semi-log representation of the same PDFs. (c) PDFs of the characteristic scale r_0 of the filament core obtained from the maxima lines which verify respectively $a_* \neq a_0$ (○) and conditions (21) (●). (d) Semi-logarithmic representation of the same PDFs. The continuous line corresponds to a linear regression fit of the data between $1\,\mathrm{cm} < r_0 < 5\,\mathrm{cm}$.

4.2 Spatial size of the filament core

In Figures 12c and 12d, we show the PDFs of the spatial size of the filament core obtained from the WT skeleton when using equations (22, 23). Actually two sets of data are represented according to the criterion one uses to select the maxima lines corresponding to the filaments namely the maxima lines for which $a_* \neq a_0$ (○) and those for which the conditions (21) are verified (●). The PDF obtained with the former maxima lines is maximum for a size $r_0 = 0.26\,\mathrm{cm}$, value which is about half the size of the transducers (0.5 cm). This histogram shows once again that a large number of these maxima lines do not correspond to a filament passing over the probe but are more likely associated with symmetrical background fluctuations with a scale a_* much too small (the minimum core size detectable experimentally should be the transducer size). The second and more realistic definition of the filaments yields a different PDF. The maximum is now reached for a value $r_0 = 0.7\,\mathrm{cm}$ very close to the transducer size and the PDF decreases much faster to 0 for values smaller than this experimental ultra-violet cutoff. The semi-log representation of both these PDFs in Figure 12d shows an exponential behavior for the values of r_0 in between 1 and 5 cm. For the maxima lines which verify equation (21), a linear regression fit of the data gives a slope equal to $0.5\,\mathrm{cm}^{-1}$ which corresponds to a characteristic scale $r_0 = 2.00 \pm 0.02\,\mathrm{cm}$. This value is quite important since it is as large as about 80 times the Taylor microscale λ ($\approx 0.025\,\mathrm{cm}$). Let us note that this estimate is much greater than the value $r_0 = 10\lambda$ obtained by Couder *et al.* [34,35] when using a simple thresholding method. This observation is not surprising since the WTMM technique allows us to detect not only the young filaments with a rather narrow core but also the burst filaments with a more complex inner structure (and therefore a not so well defined wider core). What is really surprising in the results reported in Figure 12d is that when estimating the core size of the burst filaments as explained in Section 3.3 (*i.e.* with a reference to some "average" Burgers vortex like profile), one gets values that extrapolate remarkably the exponential tail of the PDF up to values $r_0 \lesssim 6\,\mathrm{cm}$. For $r_0 \gtrsim 6\,\mathrm{cm}$, one notices some flattening of the PDF tail which suggests the existence of very wide filamentary structures. Indeed a systematic local study of these particular events shows that they correspond to maxima lines for which a_* cannot be associated to a characteristic scale of a vortical structure but rather to the distance that separates two large amplitude variations of the pressure signal that spread over some time intervals of the order of the turn-over time [82].

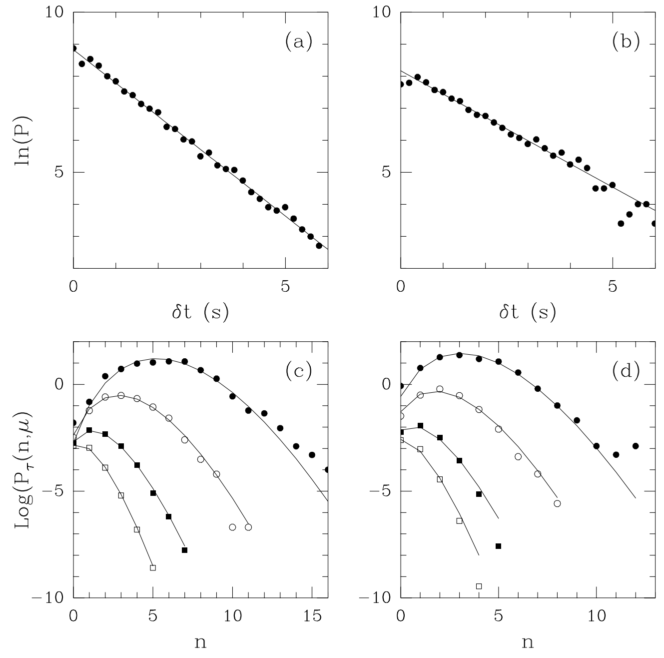

Fig. 13. Logarithm of the histogram of waiting time between (a) successive filaments with a characteristic size $r_0 < 6\,\mathrm{cm}$ and (b) successive filaments with size $1\,\mathrm{cm} < r_0 < 6\,\mathrm{cm}$. The straight lines obtained from linear regression fit have a slope equal to −1.04 and −0.73 respectively. Logarithm of the number of filaments in a window of temporal widh τ for (c) filaments of core size $r_0 < 6\,\mathrm{cm}$ and (d) filaments of core size $1\,\mathrm{cm} < r_0 < 6\,\mathrm{cm}$. The different symbols correspond to $\tau = 20T$ (●), $10T$ (○), $5T$ (■) and $2.5T$ (⊡). The continuous lines correspond to the logarithm of a Poisson's distribution (Eq. (24)) having the same mean value as the experimental distributions obtained for the previous values of τ.

4.3 Waiting time between filaments

In Figures 13a and 13b are reported the results of a statistical study of the waiting time between two successive filaments. Figure 13a shows the PDF computed for all the filaments with a core size $r_0 < 6\,\mathrm{cm}$, while Figure 13b is restricted to filaments such that $1\,\mathrm{cm} < r_0 < 6\,\mathrm{cm}$ for which the core size PDF behaves exponentially (Fig. 12d). As clearly revealed when plotting the logarithm of both these PDFs, these distributions are exponential over a wide range of waiting times $0.1\,\mathrm{s} < \delta t < 5\,\mathrm{s}$. The mean waiting time computed from linear regression fit of the data in Figures 13a and 13b is respectively $\langle \delta t\rangle \simeq 0.7\,\mathrm{s}$ and 1.45 s, values which are higher than the turn-over time $T = 0.34\,\mathrm{s}$. Thus a filament pass on the transducer every two up to four periods of rotation of the disks. Let us note that this passing frequency is higher than the value reported by Couder *et al.* in references [34,35]; this is an additional indication that our wavelet-based method allows us to detect more filaments than a simple thresholding technique that misses most of the burst filaments not associated to a deep depression. This exponential behavior of the waiting time histogram is a necessary condition to a Poisson's law characteristic of independent events. To check this possibility, let us compute the probability to detect n filaments in a window of temporal width τ. In practice, we move a window of width τ, step by step (where the step is given by the sampling time) over the whole pressure signal. At each step, we count all the events identified as a filament with our criteria (21) that belong to this window. Once the file (corresponding to 9×10^6 points) is fully processed, we repeat this operation for different values of τ to obtain the probability density $P_\tau(n,\mu)$ that can be compared to the Poisson's distribution with the same mean value μ:

$$P_\tau^{Poisson}(n,\mu) = \frac{e^{-\mu}\mu^n}{n!}\,\cdot \tag{24}$$

The comparison between the experimental distribution and the Poisson's law is shown in Figures 13c and 13d, for four temporal widths $\tau = 20T$ (●), $10T$ (○), $5T$ (■) and $2.5T$ (⊡), and for the two sets of filaments with $r_0 < 6\,\mathrm{cm}$ and $1\,\mathrm{cm} < r_0 < 6\,\mathrm{cm}$ respectively. In all cases and for all temporal window widths, the PDFs obtained are very well fitted by a Poisson's distribution. Let us point out that the agreement with the Poisson's distribution is even better when we remove from the statistics all the very narrow filaments with $r_0 < 1\,\mathrm{cm}$ [112]. Thus with our wavelet-based method, we obtain a Poisson's distribution whatever the time duration τ on the contrary to the results of Couder *et al.* [34,35] who found Poisson statistics only for values of τ larger than the turn-over time T (similar observations were reported in Refs. [37–39,42]). This discrepancy comes from the fact that a thresholding method often detects as filaments several events very close to each other corresponding to filament strands issued from the breakdown of a filament and which consequently are likely to be strongly correlated [112].

To summarize, our wavelet-based technique for filament detection allows us to detect young as well as burst filaments without particular distinction. Generally the fluctuations present in a burst filament are not identified as filaments. We show that the waiting time statistics between successive filaments passing over the probe is definitely Poisson, thereby confirming that these events are likely to be independent.

5 Multifractal analysis of the background pressure fluctuations using the WTMM method

In this section, we proceed to a multifractal analysis of the pressure signal using the WTMM method described in Section 2.3 [60,82]. Indeed our goal is to perform a comparative statistical analysis of the self-similarity properties of the overall pressure signal to those of the same experimental signal but once one has removed the vorticity filaments according to the strategy defined in Section 3.4 (see also Fig. 10). In order to be consistent with the filament selection criteria used in Section 4, we will consider two possible definitions for identifying the background pressure fluctuations:

- B1: all the maxima lines such that $a_* = a_0$.
- B2: all the maxima lines which do not verified the conditions (21).

The first definition is less accurate and in fact does not correspond to the whole "background pressure fluctuations phase". Indeed it is obvious that we have removed from the statistics a lot of maxima lines that do not correspond to a passing filament. Nevertheless with this definition we are sure that not even one of these filaments may actually pollute our statistics. The second definition contains all the background pressure fluctuations but it does not exclude the possibility that some filamentary structures may have escaped our selection criteria.

5.1 Multifractal spectra

This section is devoted to the computation of the multifractal spectra (*i.e.* the $\tau(q)$ and $D(h)$ spectra defined in Eqs. (11) and (12) respectively) of the experimental pressure signal as well as of the background pressure fluctuations B1 and B2 [82]. In Figure 14a, we show the partition function of order $q = 0$ (Eq. (10)) obtained from the WT skeleton of the whole pressure signal (●) and from the sub-skeletons corresponding to the background pressure fluctuations B1 (×) and B2 (□) when using the first order analyzing wavelet $\psi_{(3)}^{(1)}$. When plotting $\log_2(Z(0,a))$ as a function of $\log_2 a$, one gets curves that are reasonably well fitted by a straight line of slope −1 (continuous line). Thus the fractal dimension of the support of the singularities of these signals is likely to be 1: these signals are singular over intervals of finite length. Let us point out that for B1, one observes some breaking of this scaling behavior at scales $a \gtrsim 2^6$ which strongly indicates that we have removed too many maxima lines at large scale when using criterion B1. The corresponding curves $h(0,a)$ *vs.* $\log_2 a$ (Eq. (14)) are presented in Figure 14b; one obtains again a well defined scaling behavior over a scale range that extends up to some integral scale $a = 2^9$ corresponding to the turn-over time. From linear regression fit of these data, we get the following estimate for the Hölder exponent the most frequently encountered in the experimental pressure signal: $h(0) = 0.54 \pm 0.02$, *i.e.* a value significantly smaller than the theoretical prediction $h = 2/3$ derived from dimensional argument ($p \sim v^2$) when assuming the validity of K41 theory [48] which predicts the existence of a unique Hölder exponent $h = 1/3$ for the velocity field in fully developed turbulent flows. Let us point out that we get a close quantitative estimate $h(0) = 0.57 \pm 0.02$ when using the second-order analyzing wavelet $\psi_{(3)}^{(2)}$. As far as background pressure fluctuations are concerned, the most frequent Hölder exponent found for B2 is slighly smaller, $h(0) = 0.50 \pm 0.02$. More surprising is the estimate obtained for B1, $h(0) = 0.35 \pm 0.02$, which is significantly smaller than the two previous estimates and about half the theoretical value $h = 2/3$ that one can reasonably use as a reference value.

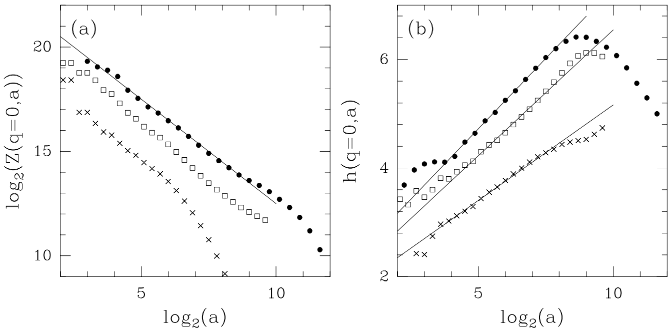

Fig. 14. Multifractal analysis of the pressure signal using the WTMM method. (a) $\log_2(Z(q=0,a))$ *vs.* $\log_2 a$ (Eq. (11)). (b) $h(q=0,a)$ *vs.* $\log_2 a$ (Eq. (14)). The different curves correspond to the results obtained with the whole pressure signal (●) and the background pressure fluctuations B1 (×) and B2 (□). The continuous lines correspond to linear regression fits of the data. The analyzing wavelet is $\psi_{(3)}^{(1)}$.

The results of the computation of the partition function $Z(q,a)$ for different values of q are shown in Figure 15a. When increasing $|q|$, oscillations become perceptible in the logarithmic representation of $Z(q,a)$ *vs.* a, which very quickly deteriorate the power-law scaling behavior observed in Figure 14a for $q = 0$. To make easier and more reliable the regression linear fit estimate of $\tau(q)$ (Eq. (11)), we will assume that $\tau(0) = -1$ (which is a reasonable assumption as the results in Fig. 14a do indicate); this will allow us to plot $\log_2(Z(q,a)/Z(0,a))$ as a function of $\log_2(a)$ in order to estimate $\tau(q)+1$. As shown in Figure 15b, when using this trick one considerably improves the scaling for the pressure signal as well as for the background pressure fluctuations B1 and B2. Indeed the more spectacular improvement is obtained for B1 and B2 for which scaling is now observed on a rather wide range of scales ($2^3 < a < 2^9$) and this for a rather large interval of q values: $-2 \leq q \leq 5$. For the pressure signal, one can however notice some breaking of this scaling behavior at scales $a \lesssim 2^4$, *i.e.* at scales smaller than the characteristic time scale $T_b = T/6 \simeq 2^6$ corresponding to the rotation period of the 6 radial blades present on the two contra-rotating disks. As shown in Figure 15b, this effect is remarkable for $q = 3$, *i.e.* for large positive q values for which the partition function $Z(q,a)$ is dominated by the contribution of the strongest singularities and very likely by the contribution of the vorticity filaments. Thus an explanation of this scale invariance breaking might simply be the fact that one is reaching scales that become comparable to the temporal characteristic size of a filament core. As previously discussed in Section 3, at scales smaller than this characteristic inner scale, a filament no longer contribute to $Z(q,a)$ as a very strong singularity of negative Hölder exponent but as a very smooth (C^∞) component. In other words, the partition function $Z(q,a)$ can be decomposed into two contributions:

$$Z(q,a) = Z^f(q,a) + Z^B(q,a)\ , \tag{25}$$

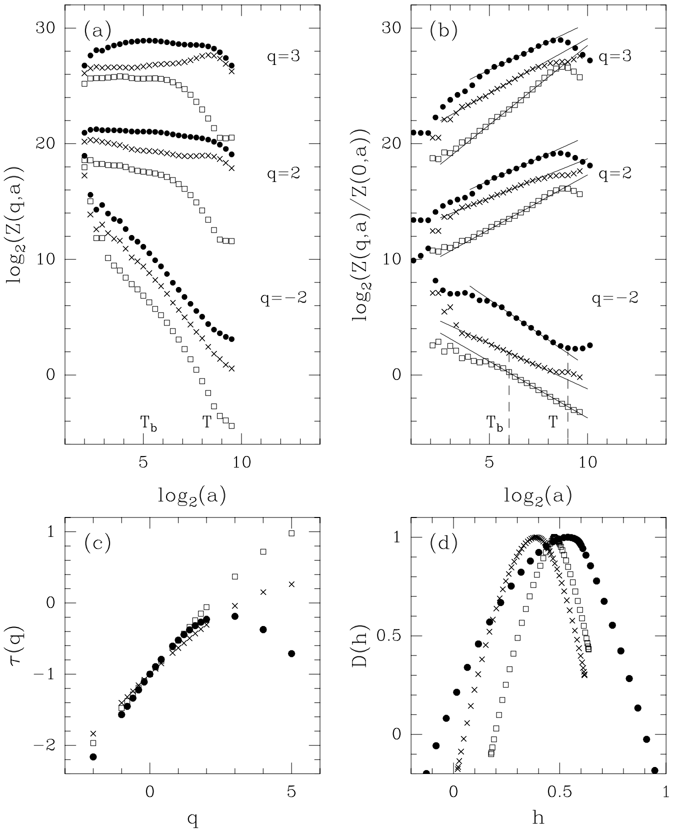

Fig. 15. Multifractal analysis of the pressure signal using the WTMM method. (a) $\log_2(Z(q,a))$ *vs.* $\log_2(a)$ (Eq. (11)). (b) $\log_2(Z(q,a)/Z(0,a))$ *vs.* $\log_2(a)$ (see text). The continuous lines correspond to the best linear regression fits obtained in the scale range $T_b \leq a \leq T$. (c) $\tau(q)$ spectrum obtained from the power-law behavior $Z(q,a)/Z(0,a) \sim a^{\tau(q)+1}$. (d) $D(h)$ singularity spectrum obtained by Legendre tranforming the $\tau(q)$ spectrum (Eq. (12)). The symbols have the same meaning as in Figure 14. The analyzing wavelet is $\psi^{(1)}_{(3)}$.

corresponding to summing over the maxima lines that belong to the WT sub-skeletons associated respectively to the "filament phase" (Fig. 10e) and to the "background pressure fluctuation phase" (Fig. 10d) [60]. From the characteristic behavior of the WT modulus along the maxima lines created by a filamentary structure (Figs. 6–8), *i.e.* some power-law increase of $|T_\psi|$ down to a scale a_* ($h \lesssim -1$) followed by some power-law decrease that depends on the order (n_ψ) of the analyzing wavelet, one does not expect $Z^f(q,a)$ to behave as a well defined power-law behavior. Moreover, as discussed in Section 4.2, the inner scale a_* actually fluctuates from one filament to the next according to their age (the oldest having the largest core size), which makes *a priori* more dramatic the influence of the filaments on the scaling properties of the pressure signal.

In Figure 15c are reported the estimate of the $\tau(q)$ spectra obtained respectively for the pressure signal and the background pressure fluctuations B1 and B2 from linear regression fit of the data in Figure 15b. The three corresponding curves are clearly nonlinear, the hallmark of multifractal signals. Nevertheless the observed curvature (concavity) is less important for B1 and B2 than for the overall pressure signal for which the $\tau(q)$ curve starts decreasing for $q \gtrsim 3$, which is the signature of the presence of very strong singularities with negative Hölder exponent ($h = \partial\tau/\partial q < 0$). Let us point out that the $\tau(q)$ curves derived from the scaling behavior of $Z^{B1}(q,a)$ and $Z^{B2}(q,a)$ (Eq. (25)), are monotonously increasing curves which indicates that our filament selection criterium has been efficient enough to get rid off the statistical contribution of the singularities with negative Hölder exponents. This can be checked in Figure 15d where the corresponding $D(h)$ singularity spectra derived by Legendre transforming the $\tau(q)$ data (Eq. (12)) are compared. The three spectra under consideration have a single humped shape characteristic of multifractal signals. The $D(h)$ spectrum for the pressure signal has a maximum equal to 1 for $h = 0.55$, consistently with the results previously shown in Figure 14. Its support extends from $h = -0.1$ to 0.9. At this point one could be confused by the fact that this support does not spread out further down to negative values of the Hölder exponent such as those observed in Figures 6, 7 and 8 ($h \simeq -1$) when detecting vorticity filaments. As investigated in Section 4.3, the characteristic waiting time between two successive recorded filaments is about 2 to 4 turn-over times, which means that one filament is not present in each realization of the process under study, as any singularity belonging to the support of the $D(h)$ spectrum should be. Along the line of Mandelbrot's argument in reference [113], one could quantify the statistical contribution of the filaments by extrapolating the $D(h)$ curve down to negative values for $h < -0.1$. From this observation, one can expect the multifractal character of the pressure fluctuations to be not so much affected when removing from the statistics the events identified as corresponding to vortex filaments. This is actually what is observed for the background pressure fluctuations B1 and B2 in Figure 15d. The $D(h)$ curve for B2 has a maximum equal to 1 for $h = 0.48 \pm 0.05$ and is narrower than the bell shape curve previously computed for the entire pressure signal. Its support $0.2 \lesssim h \lesssim 0.7$ is naturally contained in the support of the singularity spectrum of the pressure signal since each singularity involved in B2 is obviously a singularity of the pressure signal. What is more puzzling is the fact that the $D(h)$ curve obtained for B1 is shifted towards smaller values of h, $0.05 \lesssim h \lesssim 0.65$, suggesting that B1 is more singular than B2. This observation is inconsistent with the definitions of B1 and B2, since the WT sub-skeleton of B1 is entirely included in the WT sub-skeleton of B2, which implies that all the singularities involved in B1 are also present in B2. There are several possible origins to this puzzling result such as some lack of convergence in the computation of $Z(q,a)$ (especially for B1) or some intrinsic departure from scale invariance as experienced when proceeding to linear regression fit of the data for B1 and B2 in Figures 15a and 15b. We will come back to this latter point at the end of this section.

5.2 Probability density function of wavelet coefficients

In Figure 16, we show the PDFs of the increments ($\psi^{(1)}_{(0)}$) of the pressure signal ($\triangle$), and of its wavelet coefficients computed with the analyzing wavelet $\psi^{(1)}_{(3)}$ ($\blacktriangle$) for the two scales $a = 2^4$ (Fig. 16a) and 2^7 (Fig. 16b). At first glance these PDFs look like Gaussian functions. However, when plotting the logarithm of these PDFs in Figures 16c and 16d, one reveals that the tails of these distributions behave like stretched exponentials. The maximum of these PDFs is reached for $T_a = T_\psi[p](.,a) \simeq 0$, independently of the considered scale a. In Figures 16c and 16d is also represented the PDF of the WTMM of the pressure signal computed at the same scales with the same analyzing wavelet $\psi^{(1)}_{(3)}$ ($\bullet$). While the tails of this PDF still display a similar stretched exponential behavior, there exists however a main difference with the previous PDFs since, from the definition of the WTMM, this PDF is zero for $T_a = 0$. (As previously discussed in Sect. 2.3, this characteristic feature of the WTMM PDF is a key point of the WTMM method since it allows us to compute the partition function $Z(q,a)$ (Eq. (10)) for negative values of q [75–82].)

In Figures 17a and 17b, we compare the PDF of the WTMM of the pressure signal computed at a rather small scale $a = 2^4 < T_b$ ($\bullet$) with the corresponding PDFs for the background pressure fluctuations B1 ($\times$) and B2 ($\boxdot$). These latest PDFs still have stretched exponential tails but this effect is much less pronounced than for the PDF of the whole pressure signal. In Figures 17c and 17d are shown the same PDFs but at a larger scale $T_b < a = 2^7 < T$. At this scale, the removal of the maxima lines corresponding to a passing filament produces a significant change in the shape of the WTMM PDF for both B1 and B2. The continuous lines in Figures 17c and 17d correspond to a fit of the data with the following formula:

$$P(T_a) = \frac{e^{-(\ln(|T_a|^{1/2})-m)^2/2\sigma^2}}{2|T_a|}\cdot \qquad (26)$$

This expression results from the combination of the relation $p \sim v^2$ (p and v being respectivly the pressure and the velocity fields) with the results obtained in a previous analysis of wind tunnel turbulence at very high Reynolds number and which reveals that the WTMM PDF of the velocity field has a nearly log-normal shape whatever the scale selected in the inertial range [100–102,114]. Indeed equation (26) provides a remarkable fit of the WTMM PDF for both B1 and B2 in the range of scales $2^5 \lesssim a \lesssim 2^9$ previously used to estimate the $\tau(q)$ and $D(h)$ multifractal spectra. This strongly suggests that the vorticity filaments are likely to be responsible for the departure from log-normal statistics of the velocity fluctuations [82]. Furthermore the pronounced stretched exponential tails of the WTMM PDF of the overall pressure signal show that the statistical weight of the vorticity filaments is apparently more important in the low Reynolds swirling turbulent flows under study here than in wind-tunnel fully developed turbulent flows [68,75,96,100–102,114,115].

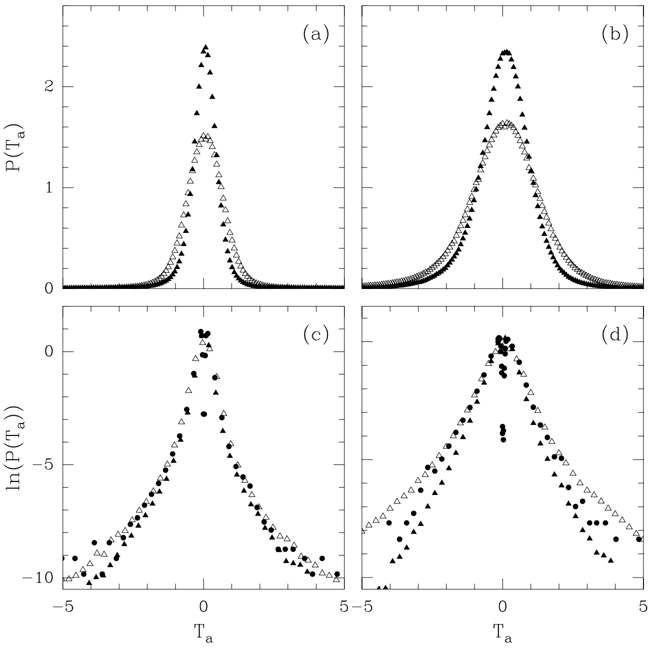

Fig. 16. Comparison of the PDF of the pressure increments ($\triangle$) with the PDF of the wavelet coefficients computed with the analyzing wavelet $\psi^{(1)}_{(3)}$ ($\blacktriangle$) for the scales $a = 2^4$ (a) and 2^7 (b). (c) and (d) correspond to the same PDFs but when using semi-logarithmic coordinates. The symbols ($\bullet$) correspond to the PDF of the WTMM computed at the same scales with the same analyzing wavelet $\psi^{(1)}_{(3)}$.

As illustrated in Figures 17a and 17b, the expression (26) does not provide such a good fit of the tails of the WTMM PDF of B1 and B2 at scale $a \lesssim 2^5$. This is probably an indication that our selection criteria for the filaments are not efficient enough at small scale. Apparently the WT sub-skeletons of B1 and B2 are somehow polluted at small scale by the presence of filamentary structures that have not been filtered out. At larger scale, equation (26) seems to be relevant, at least up to the integral scale corresponding to the turn-over time. However, when investigating the scale dependence of the parameters m and σ^2, we observe a clear departure from the expected logarithmic behavior. In fact both these parameters behave more likely as $(1-a^{-\beta})/\beta$ where $\beta \simeq 0.15$. Let us note that this exponent β somehow quantifies the departure from scale invariance ($\beta = 0$) of the background pressure fluctuations B1 and B2 observed in Figure 15a. If this observation is likely to explain the inconsistency in the $D(h)$ singularity spectrum estimates reported in Figure 15d, it rather questions the relevance of the multifractal description of the pressure fluctuations and this even once the vorticity filaments have been removed from the statistics. This result is not peculiar to the pressure fluctuations in low Reynolds swirling turbulent flows but on the contrary it corroborates the conclusions of previous analysis of high Reynolds number turbulent velocity signals [6,100–102, 114,116–122]. As reported in reference [100–102], the WT analysis of a turbulent velocity signal recorded in the

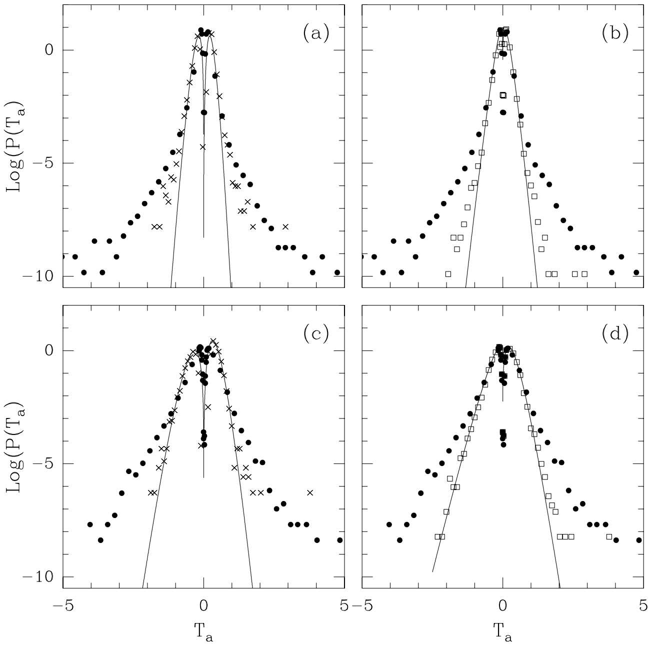

Fig. 17. Comparison of the PDF of the WTMM of the pressure signal (●) with the PDFs corresponding to the background pressure fluctuations B1 (×) and B2 (◻). The scale parameter is $a = 2^4$ for (a) and (b) and $a = 2^7$ for (c) and (d). The continuous lines correspond to a fit of the data by the expression $P(T_a) = e^{-(\ln(|T_a|^{1/2})-m)^2/2\sigma^2}/2|T_a|$ (Eq. (26)), where the parameters m and σ are estimated independently for the positive and negative parts of the considered WTMM PDF.

Modane wind tunnel at $I\!R_\lambda \simeq 2000$ brings some support to the pertinence of a self-similar log-normal cascade process to account for the intermittency phenomenon. However, this cascading process breaks scale invariance in the sense that the number of steps to go from a coarse scale a to a smaller scale a', does not behave as $\log(a'/a)$ but rather as $(a^{-\beta} - a'^{-\beta})/\beta$ [6,100–102,122], where the exponent β is found to depend on the Reynolds number. Actually β has been shown to decrease when increasing $I\!R_\lambda$ [100–102], thereby indicating that scale-invariance is likely to be restored only for very high Reynolds numbers. The possible asymptotic validity of the multifractal description *a priori* equally applies to the velocity as well as to the pressure field. Consequently one can reasonably expect that, once removed the vorticity filaments, the background pressure fluctuations (B1 and B2) possess multifractal properties in the limit $I\!R_\lambda \to +\infty$.

6 Conclusion

In this work, we have focussed our study on the low pressure tail of the PDF of pressure fluctuations recorded in a swirling turbulent flow at low Reynolds number. The corresponding pressure drops are due to the presence of vorticity filaments in the flow as evidenced by a bubble visualization technique in references [30–35]. From the ability of the WT to unfold the experimental pressure signal into a time (or space)-scale representation, we have defined a protocol to distinguish these filaments from background fluctuations. The criteria are based on the identification, in the pressure WT skeleton, of the maxima lines that correspond to strong singularities with negative Hölder exponent which are likely to be associated to vorticity filaments. This strategy actually originates from an early WT analysis of Modane wind tunnel velocity data [68,96,115]. The results reported in the present work can be seen as some experimental confirmation of the conjecture raised in this previous study. We refer the reader to Roux's thesis [82], where a complementary WT analysis of simultaneously recorded pressure and velocity signals corroborates the fact that a passing filament appears in the same way as a strong singularity with negative Hölder exponent in the velocity signal. As first tested on the Burgers vortex model, from the behavior of the pressure WT modulus along the maxima lines, one can extract the main characteristic parameters of these filaments, namely their core size and peripheral velocity. The identification of the maxima lines that correspond to a passing filament then allows us to separate the WT skeleton of the pressure signal into two sub-skeletons associated respectively to the "filament phase" and to the "background phase" of pressure fluctuations.

The investigation of the "filament" WT sub-skeleton shows that not only the young and just formed filaments are identified but also the older and so-called burst filaments. Even though the latter have a complex inner structure, they are individually identified as single isolated filamentary events. According to our selection criteria, most of the fluctuations observed in the core of these burst filaments cannot be distinguished from the background pressure fluctuations although they may correspond to thinner braided vortices also called "worms" in numerical simulations [27,29]. A statistical analysis of the "filament" WT sub-skeleton does not reveal any departure from Poisson statistics which indicates that successive vorticity filaments passing over the probe are likely to be independent events. The mean spatial core size is estimated as large as about 80 Taylor scales which is much larger than the estimate reported in previous works [34,35,39,42], *e.g.* $\sim 10\lambda$ in references [34,35] when using simple thresholding technique not so well adapted to identified burst filaments with a wide core. The mean waiting time between two successive filaments is found to be of the order of a few (2 to 4) turn-over times (*i.e* integral times). This characteristic time is not small enough to expect these filamentary structures to alter drastically the statistical properties of the background pressure fluctuations.

A statistical analysis of the scaling properties of the WT sub-skeleton corresponding to the background pressure fluctuations confirms that the statistical contribution of the vorticity filaments is not important enough to account by itself for the intermittency phenomenon. In fact, once removed all the filaments, the background pressure fluctuations display statistical properties that are compatible with the log-normal cascade process revealed in references [100–102], when investigating the fluctuations of the velocity field recorded in the Modane wind-tunnel experiment at much higher Reynolds number. In particular, when analyzing the background pressure fluctuations, one recovers some departure from scale invariance [6,100–102,116–122] which makes questionable the multifractal description of the intermittency phenomenon at finite Reynolds numbers [100–102]. There are many objective reasons that might explain our results about the lack of scaling observed when applying the WTMM method to the pressure signal. Indeed the Reynolds number is very small and the inertial range (where scaling is expected to operate) very limited. Because of the special geometrical configuration of the experimental setup, the isotropy and homogeneity hypothesis are likely to be violated. Moreover there is no mean flow and one cannot use the Taylor hypothesis to get spatial information on the pressure field. In spite of these limitations, the adequation observed between our quantitative estimate of the scale behavior of the pressure WTMM PDFs in the present study and of the velocity WTMM PDFs in the analysis of Modane wind tunnel turbulence in references [100–102], strongly suggests that the statistical contribution of vorticity filaments is not responsible for the intermittency phenomenon. This observation does not allow us to conclude that the vorticity filaments are definitely not responsible for the departure from K41 scaling theory [48]; indeed during their formation and bursting, they certainly affect and influence the neighbouring fluctuations that actually constitute the background pressure fluctuations. A decisive test would be to inhibit the physical formation of the vorticity filaments in the turbulent flow itself. Some preliminary experimental attempt in this direction (dilution of some polymer) has been performed by Bonn *et al.* [32] without further development (at least to our knowledge). There is no doubt that more experimental and theoretical work is needed before reaching a complete understanding of the physical role of vorticity filaments in turbulent flows.

We are very grateful to O. Cadot, Y. Couder and S. Douady for the permission to use their experimental turbulent signals. We acknowledge very stimulating discussions with P. Abry, B. Andreotti, E. Bacry, O. Cadot, Y. Couder, S. Douady, S. Fauve, J.F. Pinton, P. Tabeling and H. Willaime. We thank U. Frisch for bringing to our knowledge the paper of Sain *et al.* [123] where are reported evidences that vortex filaments do not affect multifractal scaling in numerical simulations of randomly forced Navier-Stokes equations. This work was supported by "Direction des Recherches, Études et Techniques" under contract (DRET n° 95/111) and by NATO (Grant n° CRG 960176).

References

1. A.S. Monin, A.M. Yaglom, *Statistical Fluid Mechanics* (MIT Press, Cambridge, MA, 1975), Vol 2.
2. U. Frisch, S.A. Orszag, *Turbulence: Challenges for Theory and Experiment*, Physics Today, 24 (1990).
3. U. Frisch, *Turbulence* (Cambridge University Press, Cambridge, 1995).
4. F. Anselmet, Y. Gagne, E.J. Hopfinger, R.A. Antonia, J. Fluid. Mech. **140**, 63 (1984).
5. Y. Gagne, thesis, University of Grenoble, 1987.
6. B. Castaing, Y. Gagne, E.J. Hopfinger, Physica D **46**, 177 (1990).
7. *Turbulence: A Tentative Dictionary*, edited by P. Tabeling, O. Cardoso (Plenum, New York, 1995).
8. A. Arneodo, C. Baudet, F. Belin, R. Benzi, B. Castaing, B. Chabaud, R. Chavarria, S. Ciliberto, R. Camussi, F. Chillà, B. Dubrulle, Y. Gagne, B. Hebral, J. Herweijer, M. Marchand, J. Maurer, J.F. Muzy, A. Naert, A. Noullez, J. Peinke, S.G. Roux, P. Tabeling, W. Van De Water, H. Willaime, Europhys. Lett. **34**, 411 (1996).
9. C. Meneveau, K.R. Sreenivasan, Nucl. Phys. B **2** (Suppl.), 49 (1987); Phys. Rev. Lett. **59**, 1424 (1987); Phys. Lett. A **137**, 103 (1989).
10. A.B. Chhabra, R.V. Jensen, Phys. Rev. Lett. **62**, 1327 (1989).
11. A.B. Chhabra, R.V. Jensen, K.R. Sreenivasan, Phys. Rev. A **40**, 4593 (1989).
12. C. Meneveau, K.R. Sreenivasan, J. Fluid Mech. **224**, 429 (1991).
13. A.N. Kolmogorov, J. Fluid Mech. **13**, 82 (1962).
14. G.K. Batchelor, A.A. Townsend, Proc. Roy. Soc. London A **199**, 238 (1949).
15. A.A. Townsend, Proc. Roy. Soc. London A **208**, 534 (1951).
16. A.Y.S. Kuo, S. Corrsin, J. Fluid Mech. **50**, 285 (1971).
17. S.C. Crow, F.H. Champagne, J. Fluid Mech. **48**, 547 (1971).
18. G.L. Brown, A. Roshko, J. Fluid Mech. **64**, 775 (1974).
19. E. Siggia, J. Fluid Mech **107**, 375 (1981).
20. K. Yamamoto, I. Hosokawa, J. Phys. Soc. Japan **57**, 1532 (1988).
21. M.E. Brachet, D.I. Meiron, S.A. Orszag, B.G. Nickel, R.H. Morf, U. Frisch, J. Fluid Mech. **130**, 411 (1983).
22. M.E. Brachet, C.R. Acad. Sci. Paris **311**, 775 (1990); Fluid. Dyn. Research **8**, 1 (1991).
23. Z.S. She, E. Jackson, S.A Orszag, Nature **344**, 226 (1990); Proc. Roy. Soc. London **434**, 101 (1991).
24. A. Vincent, M. Meneguzzi, J. Fluid Mech. **255**, 1 (1991); **258**, 245 (1994).
25. S. Kida, K. Okhitani, Phys. Fluids A **4**, 1018 (1992).
26. O. Métais, M. Lesieur, J. Fluid Mech. **239**, 157 (1992).
27. J. Jimenez, A.A. Wray, P. Saffman, R. Rogallo, J. Fluid. Mech. **255**, 65 (1992).
28. M. Tanaka, S. Kida, Phys. Fluids A **5**, 2079 (1993).
29. A. Pumir, Phys. Fluids **6**, 2071 (1993).
30. S. Douady, Y. Couder, M.E. Brachet, Phys. Rev. Lett. **67**, 983 (1991).
31. S. Douady, Y. Couder, in *Turbulence in Extended Systems*, edited by R. Benzi, C. Basdevant, S. Ciliberto (Nova Science, Commack, New York, 1993), p. 3.
32. D. Bonn, Y. Couder, P. H. J. Van Dam, S. Douady, Phys. Rev. E **47**, R28 (1993).
33. Y. Couder, S. Douady, O. Cadot, in reference [7], p. 131.
34. O. Cadot, S. Douady, Y. Couder, Phys. Fluids **7**, 630 (1995).
35. O. Cadot, thesis, University of Paris VII, 1995.
36. S. Fauve, C. Laroche, B. Castaing, J. Phys. II France **3**, 271 (1993).
37. P. Abry, S. Fauve, P. Flandrin, C. Laroche, J. Phys. II France **4**, 725 (1994).

38. P. Abry, thesis, University of Lyon I, 1994.
39. P. Chainais, DEA report (1997), unpublished.
40. E. Villermaux, B. Sixou, Y. Gagne, Phys. Fluids **7**, 2008 (1995).
41. F. Belin, J. Maurer, P. Tabeling, H. Willaime, J. Phys. II France **6**, 573 (1996).
42. B. Dernoncourt, J.F. Pinton, S. Fauve, Physica D **117**, 181 (1998).
43. G.K. Batchelor, *The Theory of Homogeneous Turbulence* (Cambridge University Press, Cambridge, 1960).
44. J. Maurer, P. Tabeling, G. Zocchi, Europhys. Lett. **26**, 31 (1994).
45. G. Zocchi, J. Maurer, P. Tabeling, H. Willaime, Phys. Rev. E **50**, 5 (1994); **50**, 3693 (1994).
46. P. Tabeling, G. Zocchi, F. Belin, J. Maurer, H. Willaime, Phys. Rev. E **53**, 1613 (1996).
47. F. Belin, P. Tabeling, H. Willaime, Physica D **93**, 52 (1996).
48. A.N. Kolmogorov, C.R. Acad. Sci. USSR **30**, 301 (1941).
49. R. Carmussi, G. Guj, Orthonormal wavelet decomposition of turbulent flows: intermittency and coherent structures, J. Fluid Mech. (1998), to appear.
50. A. Grossmann, J. Morlet, S.I.A.M. J. Math. Anal. **15**, 723 (1984); in *Mathematics and Physics, Lectures on Recent Results*, edited by L. Streit (World Scientific, Singapore, 1985), p. 135.
51. P. Goupillaud, A. Grossmann, J. Morlet, Geoexploration **23**, 85 (1984).
52. *Wavelets*, edited by J.M. Combes, A. Grossmann, P. Tchamitchian (Springer, Berlin, 1989).
53. Y. Meyer, *Ondelettes* (Herman, Paris, 1990).
54. *Les Ondelettes en 1989*, edited by P.G. Lemarié (Springer, Berlin, 1990).
55. *Wavelets and Applications*, edited by Y. Meyer (Springer, Berlin, 1992).
56. I. Daubechies, *Ten Lectures on Wavelets* (SIAM, Philadelphia, 1992).
57. *Wavelets and Their Applications*, edited by M. B. Ruskai, G. Beyklin, R. Coifman, I. Daubechies, S. Mallat, Y. Meyer, L. Raphael (Jones and Bartlett, Boston, 1992).
58. C.K. Chui, *An Introduction to Wavelets* (Academic Press, Boston, 1992).
59. *Progress in Wavelet Analysis and Applications*, edited by Y. Meyer, S. Roques (Éditions Frontières, Gif-sur-Yvette, 1993).
60. A. Arneodo, F. Argoul, E. Bacry, J. Elezgaray, J.F. Muzy, *Ondelettes, Multifractales et Turbulences: de l'ADN aux croissances cristallines* (Diderot Éditeur, Arts et Sciences, Paris, 1995).
61. *Wavelets: Theory and Applications*, edited by G. Erlebacher, M.Y. Hussaini, L.M. Jameson (Oxford University Press, Oxford, 1996).
62. M. Holschneider, *Wavelets: An Analysis Tool* (Oxford University Press, Oxford, 1996).
63. S. Mallat, *A Wavelet Tour in Signal Processing* (Academic Press, New York, 1998).
64. M. Holschneider, J. Stat. Phys. **50**, 963 (1988); thesis, University of Aix-Marseille II, 1988.
65. A. Arneodo, G. Grasseau, M. Holschneider, Phys. Rev. Lett. **61**, 2281 (1988); in reference [52], p. 182.
66. G. Grasseau, thesis, University of Bordeaux I, 1989.
67. A. Arneodo, F. Argoul, J. Elezgaray, G. Grasseau, in *Nonlinear Dynamics*, edited by G. Turchetti (World Scientific, Singapore, 1989), p. 130.
68. F. Argoul, A. Arneodo, G. Grasseau, Y. Gagne, E.J. Hopfinger, U. Frisch, Nature **338**, 52 (1989).
69. A. Arneodo, F. Argoul, G. Grasseau, in reference [54], p. 125.
70. F. Argoul, A. Arneodo, J. Elezgaray, G. Grasseau, R. Murenzi, Phys. Lett. A **135**, 327 (1989); Phys. Rev. A **41**, 5537 (1990).
71. A. Arneodo, F. Argoul, E. Bacry, J. Elezgaray, E. Freysz, G. Grasseau, J.F. Muzy, B. Pouligny, in reference [55], p. 286.
72. A. Arneodo, in reference [61], p. 349.
73. S. Mallat, S. Zhong, IEEE Trans. on Pattern Analysis and Machine Intelligence **14**, 710 (1992).
74. S. Mallat, W.L. Hwang, IEEE Trans. on Information Theory **38**, 617 (1992).
75. J.F. Muzy, E. Bacry, A. Arneodo, Phys. Rev. Lett. **67**, 3515 (1991); in reference [59], p. 323.
76. J.F. Muzy, E. Bacry, A. Arneodo, Phys. Rev. E **47**, 875 (1993).
77. E. Bacry, J.F. Muzy, A. Arneodo, J. Stat. Phys. **70**, 635 (1993).
78. J.F. Muzy, E. Bacry, A. Arneodo, Int. J. Bifurcation and Chaos **4**, 245 (1994).
79. A. Arneodo, E. Bacry, J.F. Muzy, Physica A **213**, 232 (1995).
80. E. Bacry, thesis, University of Paris VII, 1992.
81. J.F. Muzy, thesis, University of Nice, 1993.
82. S. Roux, thesis, University of Aix-Marseille II, 1996.
83. J.D. Farmer, E. Ott, J.A. Yorke, Physica D **7**, 153 (1983).
84. A. Arneodo, G. Grasseau, E.J. Kostelich, Phys. Lett. A **124**, 426 (1987).
85. P. Grassberger, R. Badii, A. Politi, J. Stat. Phys. **51**, 135 (1988).
86. T.C. Halsey, M.H. Jensen, L.P. Kadanoff, I. Procaccia, B.I. Shraiman, Phys. Rev. A **33**, 1141 (1986).
87. P. Collet, J. Lebowitz, A. Porzio, J. Stat. Phys. **47**, 609 (1987).
88. T. Bohr, T. Tèl, in *Direction in Chaos*, edited by B.L. Hao (World Scientific, Singapore, 1988), Vol. 2.
89. G. Parisi, U. Frisch, Fully developed turbulence and intermittency, in Proc. of Int. School on *Turbulence and Predictability in Geophysical Fluid Dynamics and Climate Dynamics*, edited by M. Ghil, R. Benzi, G. Parisi (North-Holland, Amsterdam, 1985), p. 84.
90. A. Arneodo, E. Bacry, J.F. Muzy, Phys. Rev. Lett. **74**, 4823 (1995).
91. A. Arneodo, E. Bacry, S. Jaffard, J.F. Muzy, J. Stat. Phys. **87**, 179 (1997); J. Fourier Analysis and Applications (1997), to appear.
92. A. Arneodo, E. Bacry, S. Jaffard, J.F. Muzy, C.R.M. Proceedings and Lecture Notes **17**, 99 (1998).
93. S. Jaffard, C. R. Acad. Sci. Paris, t. 308, serie I, 79 (1989).
94. M. Holschneider, P. Tchamitchian, in reference [54], p. 102.
95. D. Sornette, in *Scale Invariance and Beyond*, edited by B. Dubrulle, F. Graner, D. Sornette (Springer, EDP Sciences, 1997), p. 235.
96. E. Bacry, A. Arneodo, U. Frisch, Y. Gagne, E.J. Hopfinger, in *Turbulence and Coherent Structures*, edited by M. Lesieur, O. Metais (Kluwer, Dordrecht, 1991), p. 203.
97. M. Vergassola, R. Benzi, L. Biferale, D. Pisarenko, J. Phys. A **26**, 6493 (1993).
98. M. Vergassola, U. Frisch, Physica D **54**, 58 (1991).

99. S. Jaffard, Multifractal Formalism for functions, Parts I and II, SIAM J. Math. Analysis (1997), to appear.
100. A. Arneodo, J.F. Muzy, S. Roux, J. Phys. II France **7**, 363 (1997).
101. A. Arneodo, S. Manneville, J.F. Muzy, S.G. Roux, Applied and Computational Harmonic Analysis (1998), to appear.
102. A. Arneodo, S. Manneville, J.F. Muzy, Eur. Phys. J. B **1**, 129 (1998).
103. A. Arneodo, E. Bacry, P.V. Graves, J.F. Muzy, Phys. Rev. Lett. **74**, 3293 (1995).
104. A. Arneodo, Y. D'Aubenton-Carafa, E. Bacry, P.V. Graves, J.F. Muzy, C. Thermes, Physica D **96**, 291 (1996).
105. A. Arneodo, Y. D'Aubenton-Carafa, B. Audit, E. Bacry, J.F. Muzy, C. Thermes, Eur. Phys. J. B **1**, 259 (1998); Physica A **249**, 439 (1998).
106. A. Arneodo, J.P. Bouchaud, R. Cont, J.F. Muzy, M. Potters, D. Sornette, preprint cond-mat/9607120 at http://xxx.lanl.gov.
107. A. Arneodo, J.F. Muzy, D. Sornette, Eur. Phys. J. B **2**, 277 (1998).
108. A. Arneodo, F. Argoul, E. Bacry, J.F. Muzy, M. Tabard, Phys. Rev. Lett. **68**, 3456 (1992); Fractals **1**, 629 (1993).
109. A. Arneodo, F. Argoul, J.F. Muzy, M. Tabard, Phys. Lett. A **171**, 31 (1992); Physica A **188**, 217 (1992).
110. P. Lévy, *Processus Stochastiques et Mouvement Brownien* (Gauthiers-Villars, 1965).
111. B.B. Mandelbrot, J.W. Van Ness, SIAM Rev. **10**, 422 (1968).
112. Note that most of the filament strands that come out from the breakdown of the same filament have a width $r_0 < 1\,\mathrm{cm}$ and are likely to be correlated.
113. B.B. Mandelbrot, Pure Appl. Geophys. **131**, 5 (1989); Physica A **163**, 306 (1990).
114. A. Arneodo, B. Audit, E. Bacry, S. Manneville, J.F. Muzy, S. Roux, in *Scale Invariance and Beyond*, edited by B. Dubrulle, F. Graner, D. Sornette (Springer – EDP Sciences, 1997), p. 37.
115. A. Arneodo, E. Bacry, J.F. Muzy, in reference [7], p. 139.
116. B. Castaing, Y. Gagne, M. Marchand, Physica D **68**, 387 (1993).
117. A. Naert, L. Puech, B. Chabaud, J. Peinke, B. Castaing, B. Hébral, J. Phys. II France **4**, 215 (1994).
118. B. Chabaud, A. Naert, J. Peinke, F. Chillà, B. Castaing, B. Hébral, Phys. Rev. Lett. **73**, 3227 (1994).
119. B. Castaing, B. Dubrulle, J. Phys. II France **5**, 895 (1995).
120. B. Castaing, J. Phys. II France **6**, 105 (1996).
121. F. Chillà, J. Peinke, B. Castaing, J. Phys. II France **6**, 455 (1996).
122. B. Castaing, in *Scale Invariance and Beyond*, edited by B. Dubrulle, F. Graner, D. Sornette (Springer – EDP Sciences, 1997), p. 225.
123. A. Sain, M. Pandit, R. Pandit, Turbulence and multiscaling in the randomly forced Navier-Stokes equations, preprint Indian Institute of Science, Bangalore (Dec. 1997).